Astronomy & Astrophysics manuscript no. output
July 14, 2026

Trading oxygen for iron

II. Oxygen- versus iron-dependent cosmic star formation history

M. Chruślińska[1,2], M. Curti[1], R. Pakmor[2], A. De Cia[1], J. Matthee[3], A. Bhagwat[2], S. Monty[4,5]

[1] European Southern Observatory, Karl-Schwarzschild-Str. 2, 85748 Garching, Germany
[2] Max Planck Institute for Astrophysics, Karl-Schwarzschild-Str. 1, D-85748 Garching, Germany
[3] Institute of Science and Technology Austria, Am Campus 1, 3400 Klosterneuburg, Austria
[4] Center for Interdisciplinary Exploration and Research in Astrophysics (CIERA), Northwestern University, 1800 Sherman Avenue, Evanston, IL 60201, USA
[5] Department of Astronomy, New Mexico State University, Las Cruces, NM 88003, USA

Received November , 2025; accepted XX XX, 2025

ABSTRACT

Due to their different nucleosynthetic origin, a stellar population produces oxygen (O) and iron (Fe) on different timescales, and their relative abundance can deviate strongly from solar. Galaxy formation models should treat these elements separately, as they play a distinct role in shaping physical phenomena. For example, oxygen mainly sets the gas cooling rate, while the iron abundance sets stellar atmosphere opacities impacting stellar evolution, spectra, and feedback. Observations of star-forming galaxies usually only constrain gas-phase oxygen abundance, vastly limiting our capabilities of separating the cosmic evolution of oxygen and iron. Here, we present an observationally motivated framework to scale the cosmic evolution of O and Fe abundances. We applied the relation between the α-enhancement and galaxies' specific star formation rate ([O/Fe]–sSFR) to derive the Fe and O-dependent cosmic star-formation history (cSFH). We find that star formation with near-solar O/Fe is rare: at least 70% of the integrated cosmic stellar mass forms at non-solar O/Fe. The cosmic average metallicity is generally lower in [Fe/H] than in [O/H] (by up to a factor 3), with the offset increasing from $z = 0$ to redshifts $z \approx 3$ and then approaching the core-collapse O/Fe ratio. We validated our results against samples that probed the Fe-dependent cSFH in different regimes such as absorption-derived $\langle$[Fe/H]$\rangle$ from long gamma-ray bursts. Our results impact the interpretations of stellar and galaxy spectra and the predicted rates of transients, especially those linked to metal-poor progenitors (e.g. black hole mergers).

Key words. Stars: abundances, formation - Galaxies: abundances, evolution, star formation

1. Introduction

The chemical composition of material within galaxies evolves as nucleosynthetic products from stars are ejected and mixed into the surrounding medium. Increasing metallicity (abundance of elements heavier than helium) alters the physics and observable properties of both stars (Garcia et al. 2021; Eldridge & Stanway 2022; Vink 2022) and galaxies (Bromm & Loeb 2003; Maiolino & Mannucci 2019; Kewley et al. 2019), but not all elements affect evolution equally. Among them, oxygen and iron provide a striking example: they regulate different key processes, and their abundances evolve on different timescales. Oxygen largely sets gas cooling, regulating how efficiently gas is converted into stars (Bromm & Loeb 2003; Richings et al. 2014; Katz et al. 2022; Sharda et al. 2023); iron-group elements control stellar opacities and radiation-driven winds (Iglesias & Rogers 1996; Vink et al. 2001), shaping stellar lives and deaths (Puls et al. 2008; Langer 2012; Smith 2014; Meynet et al. 2015; Heger et al. 2023), transient formation and properties (Langer & Norman 2006; Belczynski et al. 2010b; Perley et al. 2016; Schulze et al. 2018; Chruślińska 2024), ionising-radiation output (e.g. Leitherer et al. 1999; Stanway & Eldridge 2018; Götberg et al. 2019, 2020), and feedback on galactic scales (Eldridge & Stanway 2022). Oxygen is produced by sources linked to massive stars and is released promptly after star formation (Woosley et al. 2002; Heger et al. 2003; Janka et al. 2007; Schneider et al. 2021; Kobayashi & Taylor 2023). Iron additionally has a substantial contribution from type Ia supernovae (Tinsley 1979; Nomoto et al. 1997; Maoz et al. 2014; Kobayashi et al. 2020) with a wide delay-time distribution (DTD) (Nomoto 1982; Iben & Tutukov 1984; Webbink 1984; Greggio 2005; Maoz & Mannucci 2012; Wang & Han 2012; Maoz et al. 2014; Livio & Mazzali 2018). Consequently, their relative abundance can depart from the solar ratio by a factor of $\gtrsim 5$ (Matteucci & Greggio 1986; Wheeler et al. 1989; Kobayashi & Taylor 2023; Chruślińska et al. 2024; Monty et al. 2025). Observations of star-forming galaxies typically constrain only oxygen, which is the most abundant metal with strong emission lines (Maiolino & Mannucci 2019) available for growing samples across redshifts (Nakajima et al. 2023; Chemerynska et al. 2024; Curti et al. 2024; Revalski et al. 2024; Sanders et al. 2024). By contrast, the iron abundance in star-forming gas is particularly difficult to determine (e.g. due to faint lines and strong dust depletion) and will likely remain unavailable for representative samples in the near term (Chruślińska et al. 2024). Consequently, oxygen abundance is often used as a proxy for it, assuming a scaling that maintains relative abundance ratios as determined for the Sun. This can introduce significant and yet unaccounted-for errors. Here, we

Article published by EDP Sciences, to be cited as https://doi.org/10.1051/0004-6361/202558246

propose a method to address this issue.
In Paper I, Chruślińska et al. (2024) (Ch24) introduced the relation between the oxygen-to-iron abundance ratio and the specific star formation rate of galaxies ([O/Fe]–sSFR relation) as an effective to translate oxygen to iron abundances. Ch24 showed that the relation is supported by both cosmological simulations (Schaye et al. 2015; Crain et al. 2015; Weinberger et al. 2017; Pillepich et al. 2018) and basic theoretical expectations (see also Matthee & Schaye 2018; Kashino et al. 2022). They used a homogenised sample of star-forming galaxies to provide empirical constraints. Here, we applied this relation to infer the iron-dependent cosmic star formation history (cSFH), $f_{\rm SFR}(Z_{\rm Fe/H}, t)$ and compared it with its oxygen-based counterpart, $f_{\rm SFR}(Z_{\rm O/H}, t)$. To this end, we expand and update the framework developed in Chruślińska & Nelemans (2019) (ChN19) and Chruślińska et al. (2021) (Ch21), which estimates $f_{\rm SFR}(Z_{\rm O/H}, t)$ by combining empirical distributions of galaxy properties (e.g star formation rate or SFR, gas-phase oxygen abundance $Z_{O/H}$, and stellar mass M_*) with number statistics while propagating the associated uncertainties. As a verification step, we compared our $f_{\rm SFR}(Z_{\rm Fe/H}, t)$ predictions with samples of Milky Way (MW) globular clusters (GCs) (Carretta et al. 2009; VandenBerg et al. 2013) and RR Lyrae stars in local dwarfs (Bellazzini et al. 2025), which probe different parts of the cosmic star formation rate distribution in iron (Sect. 3.2). In Sect. 6 we further compare our results with the absorption-based cosmic star formation rate density (SFRD)-weighted average metallicity probed by long gamma-ray bursts (LGRBs; Heintz et al. 2023). Where appropriate, we adopted a standard flat cosmology with $\Omega_{\rm M} = 0.3$, $\Omega_\Lambda = 0.7$ and $H_0 = 70$ km s^{-1} Mpc^{-1} (Hinshaw et al. 2013) and assumed a Kroupa (2001) initial mass function (IMF). The terms 'redshift' (z), 'cosmic time' (t), and 'look-back time' are used interchangeably throughout the paper (z= look-back time = 0 at present day), and the relation between them is fixed within the assumed cosmological model. We used the solar reference abundances from Grevesse & Sauval (1998) for consistency with previous work (12+log$_{10}$(O/H)$_\odot$=8.83, 12+log$_{10}$(Fe/H)$_\odot$=7.5, log$_{10}$(O/Fe)$_\odot$=1.33). Where necessary, we shifted the abundances from literature samples to this solar reference scale. Different solar reference values are reported and used across the literature (especially for oxygen different estimates differ by ~0.15 dex; e.g. Lodders et al. 2009; Asplund et al. 2009, 2021). This choice only affects the numerical results reported for the abundances relative to solar. Where these results cannot be straightforwardly converted to a different solar reference, we comment on the impact this has. We use the following notation to distinguish between absolute and solar-relative abundances: $Z_{X/H}$=12+log$_{10}$(X/H) for absolute abundances, and [X/H] = $Z_{X/H}$ - $Z_{X/H;\odot}$ for abundances relative to solar, where the index 'X=O' refers to oxygen and 'X=Fe' to iron.

2. Method: Trading oxygen for iron using the [O/Fe]– sSFR relation of galaxies

We aim to self-consistently derive and compare the oxygen-based $f_{\rm SFR}(Z_{O/H},t)$ and iron-based $f_{\rm SFR}(Z_{Fe/H},t)$. We followed the phenomenological approach detailed in ChN19 and Ch21. The key additional step introduced in this work is the application of the [O/Fe]–sSFR relation of galaxies from Ch24, which allows us to estimate $f_{\rm SFR}(Z_{Fe/H},t)$. The core idea of our framework is summarised below, while further details can be found in Appendix A. Our approach requires knowledge of the following main ingredients:

1) [O/Fe]–specific SFR relation (redshift invariant);
2) Distribution of sSFR of galaxies as a function of redshift;
3) (a) Distribution of $Z_{O/H}$ of galaxies;
(b) Relation linking galaxy $Z_{O/H}$ and sSFR;
(c) Evolution of (3a) and potentially (3b) with redshift;
4) Number density of galaxies n_{gal} with different sSFR and $Z_{O/H}$ as a function of redshift.

These are illustrated in Fig. 1 (2-4), Fig. 2 (1), and Fig. 3 (3c). In ChN19; Ch21, (2-4) were determined based on a compilation of observational studies and extrapolated where necessary. Distributions (2) and (3a) were characterised as a function of the galaxy's stellar mass M_*. At a fixed z, galaxies follow a ridge in the $Z_{O/H}$–log$_{10}(M_*)$ plane with characteristic scatter σ_{MZR} in $Z_{O/H}$, referred to as the mass–metallicity relation (MZR; grey line in the bottom panel in Fig. 1; e.g. Tremonti et al. 2004; Maiolino et al. 2008; Curti et al. 2020; Sanders et al. 2021; Nakajima et al. 2023; Curti et al. 2024; Scholte et al. 2024, see the review by Maiolino & Mannucci 2019). We obtained the distribution of sSFR (middle panel in Fig. 1) starting from the distribution of galaxies observed in the log$_{10}(SFR)$ - log$_{10}(M_*)$ plane. The main ridge in this plane defines the galaxy main sequence (e.g. Brinchmann et al. 2004; Speagle et al. 2014; Tomczak et al. 2016; Popesso et al. 2023; Simmonds et al. 2025; Di Cesare et al. 2026) with a characteristic scatter σ_{SFR}=0.3 dex. For consistency with earlier work, the galaxy main sequence is referred to as the star formation—mass relation (SFMR) throughout the paper. A bimodality in the log$_{10}(SFR)$ - log$_{10}(M_*)$ plane is sometimes observed, with the secondary ridge occupied by starburst (SB) galaxies and referred to as the SB sequence (e.g. Rodighiero et al. 2011; Sargent et al. 2012; Schreiber et al. 2015; Caputi et al. 2017; Rinaldi et al. 2025). If $Z_{O/H}$ and SFR (sSFR) were not correlated, these galaxy properties could be easily connected via M_*. In general this is not the case, and the additional relation linking $Z_{O/H}$, SFR and M_* (3b) takes into account the observed anti-correlation between the galaxy's $Z_{O/H}$ and sSFR. This is known as the fundamental metallicity relation (FMR; see bottom panel in Fig. 1 e.g. Ellison et al. 2008; Mannucci et al. 2010, 2011; Yates et al. 2012; Andrews & Martini 2013; Lara-López et al. 2010; Sanders et al. 2018; Curti et al. 2020). The FMR is found to be z-invariant in the models and simulations (Davé et al. 2011; Lagos et al. 2016; De Rossi et al. 2017; Torrey et al. 2018, but see Garcia et al. 2024) and is consistent with no evolution according to observations (e.g. Cresci et al. 2019; Sanders et al. 2021) at least up to z~3. If the FMR is z-invariant, (3c) the evolution of galaxy $Z_{O/H}$ with z is determined by the evolution of other galaxy properties. However, recent studies have obtained conflicting results regarding the FMR and its universality in the early Universe (e.g. Heintz et al. 2023; Langeroodi & Hjorth 2023; Nakajima et al. 2023; Curti et al. 2023, 2024, identify z≳6 galaxies showing significant departures from the z=0 FMR) and at low $M_* \lesssim 10^9 M_\odot$ (Kotiwale et al. 2026; Laseter et al. 2025). We note that $Z_{O/H}$ at z≳3 (and 3c) were essentially unconstrained prior to JWST, and the work of ChN19; Ch21 rely on different extrapolations in this regime. In Sect. 2.2 we review our assumptions in light of these new observational results and rule out some of these extrapolations, making a crucial update to our framework.
Once (2) and (3) were fixed, the $Z_{Fe/H}$ of each galaxy (characterised by z, M_*, $Z_{O/H}$ and SFR) was estimated using (1) (see Sect. 2.1 and Fig. 2). Following ChN19, we accounted for the fact that star formation in a galaxy occurs over a range of metallicities by distributing the SFR as a Gaussian

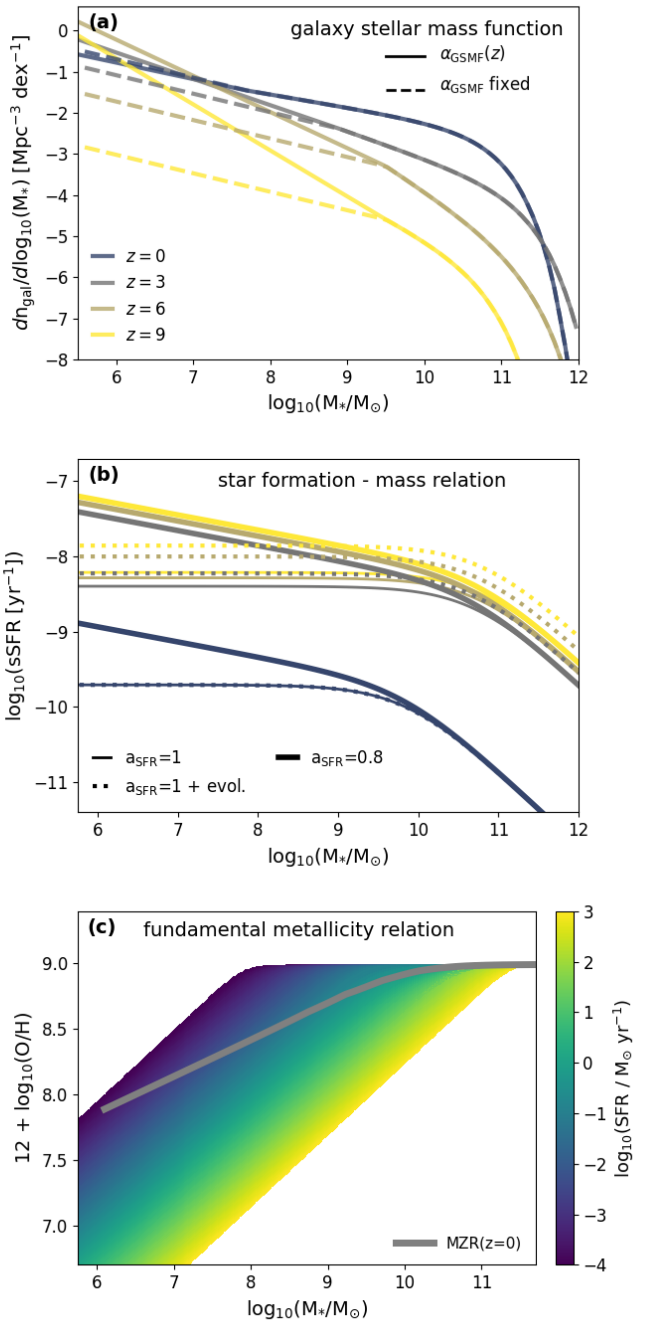

Fig. 1. GSMF (top panel), showing the number density of galaxies as a function of M_*, and the scaling relations linking the galaxy properties used in our framework: the sSFR–M_* relation (middle panel; derived from the P23 SFMR) and the joint dependence of $Z_{O/H}$, SFR, and M_*, shown as a 2D projection of the redshift-invariant FMR (bottom panel), which also includes the $z \sim 0$ MZR. The colours in the top and middle panels indicate different redshifts, illustrating the evolution of these relations. The different line styles in the top and middle panels show considered variations in the assumed low-M_* slope and redshift evolution of the relations (see Appendix B). The evolution of the $Z_{O/H}$ scaling relations is shown in Fig. 3.

centred on the $Z_{\rm O/H}$ and $Z_{\rm Fe/H}$ values derived from the scaling relations. For simplicity, we adopted a common dispersion, $\sigma_{\nabla \rm O/H} = \sigma_{\nabla \rm Fe/H} = 0.14$ dex, with the value guided by the observed $Z_{\rm O/H}$ distribution in HII–regions of $z \sim 0$ disk galaxies (Sánchez-Menguiano et al. 2016, 2017, see appendix C for additional discussion). The purpose of step (4) is to provide a 'weighting factor', accounting for the fact that galaxies with different properties contribute unequally to the cosmic star formation budget due to their varying abundances in the cosmic volume. All relevant galaxy properties in our framework can be linked via M_*, and the weighting $n_{gal}(M_*,z)$ was obtained from the galaxy stellar mass function (GSMF; top panel in Fig. 1, e.g. Baldry et al. 2012; Muzzin et al. 2013; Stefanon et al. 2021). The product of (2) and (4) integrated over the full relevant range of M_* ($10^6 - 10^{12} M_\odot$ in this work) gives the total SFRD (i.e. at all metallicities). The result of this integration as a function of z gives the cSFH (Sect. 5.1). By summing only the contribution of galaxies with a given $Z_{O/H}$ or $Z_{Fe/H}$, we derived the SFRD as a function of metallicity, i.e. either oxygen- or iron-based metallicity-dependent cSFH. See Appendix A for the derivation.

For our initial estimate, we assumed:
(1) The [O/Fe]–sSFR relation corresponding to the 'mixed' Fe enrichment variation defined in Sect. 2.1.
(2) The SFMR from Popesso et al. (2023) (P23), based on a homogenised set of observational literature estimates spanning $0 < z < 6$ but with additional evolution in the normalisation at high z (dotted lines in the middle panel in Fig. 1). This modification is motivated by the recent results of Simmonds et al. (2025), constraining the SFMR up to $z \sim 9$. Table B.1 (row '$a_{\rm SFR}$=1+ evol.') provides the implementation details. We included a small fraction of SB (f_{SB}=3%, as in Boco et al. 2021,Ch21), which yields negligible SB contribution to the cSFH (see Appendix A.6 for further details).
(3a) The MZR(z = 0) matching Curti et al. (2020) with the asymptotic value at high M_* ($Z_{O/H;\rm MZR0}$) shifted by +0.2 dex (grey line in the bottom panel in Fig. 1; see Table B.1 for details). Ch24 show that such a systematic shift in $Z_{O/H}$ estimated from electron temperature-sensitive auroral lines (and the derived strong line calibrations, including Curti et al. 2020) may be necessary to reconcile the average [O/Fe] of young star-forming galaxies and old MW stars.
(3b) The FMR as described in Ch21 (colour-mapped in the bottom panel in Fig. 1) and determined by MZR(z = 0), SFMR(z = 0), and a parameter $\nabla_{\rm FMR0}$, characterising the strength of the $Z_{O/H}$–SFR correlation at high SFR and low to intermediate M_*[1] (see Appendix A.4 for further details). We used $\nabla_{\rm FMR0} = 0.27$ as in Ch21.
(3c) A fixed FMR at $z \leqslant 3$ and an FMR with decreasing normalisation at $z > 3$, as discussed in Sect. 2.2. This accounts for the potential additional $Z_{O/H}$ evolution beyond that resulting from a z-invariant FMR, as allowed by current observational constraints.
(4) The GSMF from ChN19 extrapolated to low $M_*=10^6 M_\odot$ with a z-dependent slope $\alpha_{\rm GSMF}(z)$ and updated to include more recent results (solid lines in top panel in Fig. 1), as described in Appendix A.5.
We refer to the model characterised by the above choices (1–4) as the 'example variation'. We use this in Sect. 3 to discuss the main characteristics of our results with further detail. In Sect. 4 and beyond, we also explore alternative assumptions to assess the sensitivity of our results to these choices. The variations, summarised in Table B.1 in Appendix B, were selected to capture the major uncertainties in our framework while remaining broadly consistent with current constraints

[1] δMZR = -$\nabla_{\rm FMR0} \cdot \delta$SFMR, where δMZR and δSFMR are the galaxy's offsets from the respective relations.

on the [O/Fe]–sSFR relation (Sect. 2.1), MZR (Sect. 2.2), and cSFH (Sect. 5.1).

2.1. The relation between [O/Fe]–specific SFR

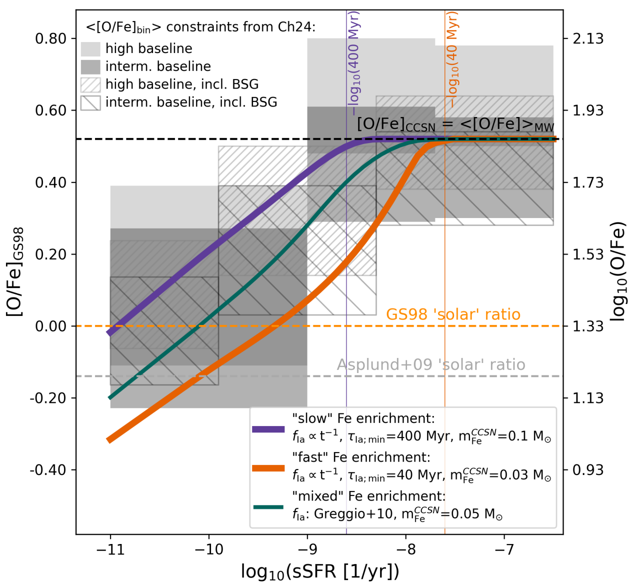

Fig. 2. [O/Fe]–sSFR relation of galaxies. The coloured lines show the three model variations considered in this paper: 'slow' Fe enrichment (purple), 'fast' Fe enrichment (orange), and 'mixed' Fe enrichment (green). These variations span the range permitted by the observational constraints discussed in Ch24 and shown as solid and hatched areas (see text for the details). The horizontal black line indicates the average abundance ratio of the MW thick disk and halo dwarf stars with [Fe/H] <–2 from Amarsi et al. (2019). The horizontal orange line indicates our reference solar $\log_{10}(O/Fe)|_\odot$=1.33 dex (Grevesse & Sauval 1998). The zero point on the Asplund et al. (2009) solar scale is shown as a dashed grey line.

Figure 2 summarises the constraints on the [O/Fe]–sSFR relation derived by Ch24, who also show that most current theoretical expectations are consistent with these constraints. These constraints were obtained after homogenising the $Z_{O/H}$ and $Z_{Fe/H}$ measurements of star-forming galaxies, which were compiled from the literature and binned using the sSFR. They are illustrated as grey boxes in Fig. 2, which show the [O/Fe] values in three $\log_{10}$(sSFR) bins and span the 0.13–99.87 percentiles of the mean [O/Fe] in each bin. Ch24 homogenised oxygen and iron abundances by correcting for known average systematic offsets (putting them on a 'common baseline') and excluding cases that cannot be consistently treated. All abundances were first converted to a common solar reference scale (Grevesse & Sauval 1998), removing offsets of up to $\gtrsim$0.14 dex arising from differences in the adopted solar abundances. For oxygen, only H II-region-based estimates were used, relying either on temperature-sensitive emission lines or on empirically calibrated strong-line diagnostics tied to such measurements. Some literature values include additional systematic shifts, in particular corrections of ≈0.2−0.24 dex to place abundances on the recombination-line scale, or dust depletion corrections of typically ≈0.1 dex. Ch24 either removed these corrections or uniformly applied them to all data, depending on the chosen common baseline. For iron, the methods used in the literature are less uniform, and the associated systematics are less well quantified than for oxygen. Ch24 restricted their analysis to $Z_{Fe/H}$ estimates derived either from the spectra of young stars or from rest-frame UV spectra of galaxies. The latter depend on the adopted stellar population synthesis (SPS) models, with an average difference of ≈ 0.1 dex between the values derived using Starburst99 (Leitherer et al. 1999) and BPASS (Stanway et al. 2016; Stanway & Eldridge 2018, i.e. the two most commonly used SPS libraries in the compiled datasets). All of these systematics were accounted for using either the average offsets listed above or, where available, the exact values reported in the original studies (see Table E.1 in Ch24). Ch24 defined several common baseline choices. In Fig. 2, we only show those for which the high sSFR 'plateau' of the [O/Fe]–sSFR relation is at the value consistent with the average $<$[O/Fe]$>_{MW}$ of old metal-poor MW stars. These values are expected to be similar, reflecting the integrated yields of massive, metal-poor stars and the associated core-collapse supernovae (CCSNe), which eject material with supersolar O/Fe, prior to significant enrichment from delayed sources. The hatched boxes show the (tighter) constraints derived assuming that blue supergiant (BSG)-based metallicity (Bresolin et al. 2016, 2022) can be used as a measure of galaxy's $Z_{Fe/H}$. The coloured lines in Fig. 2 represent three model variations of the [O/Fe]–sSFR relation, which span these constraints. These relations were computed following Eq. 1 from Ch24, recalled below:

$$[O/Fe] = [O/Fe]_{CCSN} - \log_{10}\left(1 + \frac{m_{Fe}^{Ia}}{m_{Fe}^{CCSN}} \frac{N_{Ia0}}{k_{CCSN}} \frac{\int_0^t SFR(t')f_{Ia}(t-t')\,dt'}{SFR}\right), \quad (1)$$

where $[O/Fe]_{CCSN}$ sets the oxygen-to-iron abundance ratio relative to solar in the high sSFR regime dominated by CCSN enrichment, m_{Fe}^{CCSN} and m_{Fe}^{Ia} are the average iron masses ejected per CCSN and SN Ia event, k_{CCSN} is the CCSN formation efficiency (number of CCSNe per unit stellar mass formed), N_{Ia0} is the SN Ia formation efficiency (i.e. the Hubble time-integrated number of SN Ia formed per unit stellar mass), and f_{Ia} is the SN Ia DTD, normalised to unity over the Hubble time. We stress that these parameters should be understood as effective quantities and that their direct interpretation in terms of supernova yields or specific enrichment channels is not straightforward. Equation 1 simply provides a convenient parametrisation that captures the main features of the relation and preserves its connection to delayed iron enrichment relative to oxygen – the primary physical driver.

Using cosmological simulations of galaxy evolution (EAGLE Crain et al. 2015; Schaye et al. 2015; McAlpine et al. 2016 and TNG Weinberger et al. 2017; Pillepich et al. 2018; Nelson et al. 2019) in Paper I, Ch24 demonstrated that the average [O/Fe]–sSFR relation can be reproduced with Eq. 1 using fixed effective values of the iron yields (m_{Fe}^{CCSN}, m_{Fe}^{Ia}) and the average abundance $[O/Fe]_{CCSN}$ (see Sect. 2.5 and Fig. 4 therein). This holds despite the fact that these simulations adopted different metallicity-dependent yield tables and included additional processes (e.g. galaxy mergers and gas flows) that can affect chemical evolution of individual galaxies. In these examples, the assumed metallicity-dependent yields and CCSN progenitor mass range affect mostly the effective normalisation $[O/Fe]_{CCSN}$. Ch24 identify SN Ia DTD and the relative iron production rate in SN Ia compared to CCSNe, $C_{Ia/CC} := \frac{m_{Fe}^{Ia}}{m_{Fe}^{CCSN}} \frac{N_{Ia0}}{k_{CCSN}}$, as the main factors controlling the shape of the relation. These parameters can be understood more broadly as a delay in the enhanced iron production (whether arising from SN Ia, low-mass CCSNe, or both) and the relative efficiency of prompt and delayed iron and oxygen enrichment channels. As the underlying nucleosynthetic processes do not depend on redshift, the average [O/Fe]–sSFR relation is not expected to evolve. However, galaxy populations at different redshifts are expected to occupy different regions of the [O/Fe]–sSFR plane: at higher redshifts, galaxies are typically younger and have higher sSFR (see middle panel in Fig. 1), with chemical enrichment dominated by massive-star progenitors. They thus exhibit, on average, higher [O/Fe] ratios than galaxies at lower redshifts.

Following Ch24, we fixed $[O/Fe]_{CCSN}$=<[O/Fe]>$_{MW}$=0.52 dex[2] to match the average abundance ratio of metal-poor MW stars from Amarsi et al. 2019 (used as a baseline for their careful treatment of non-local thermodynamic equilibrium effects). The flattening at $[O/Fe]_{CCSN}$ at the high-sSFR end of the relation is analogous to that found for MW stars at low [Fe/H] in conventional Tinsley–Wallerstein diagrams (showing stellar [Fe/H] vs their enhancement in α-elements; Wallerstein 1962; Tinsley 1979). However, the very low [Fe/H]$\lesssim$-2.5 regime is poorly constrained by observations. Detailed galaxy chemical evolution models often predict a gradual change of slope at high [O/Fe] (e.g. Matteucci 2021) rather than a strict plateau (as in Eq. 1). In this view, our results may underestimate [O/Fe] and the low-Fe tail of the $f_{SFR}(Z_{Fe/H}, t)$ at high redshifts. On the other hand, rare transients associated with very massive, metal-poor stars (e.g. pair-instability supernovae Heger & Woosley 2002 or certain hypernova scenarios Grimmett et al. 2021) can produce ejecta with significantly lower [O/Fe] than standard CCSNe. If such events occur with non-negligible frequency, they would introduce additional scatter and potentially a population of outliers below the high-sSFR plateau that are not accounted for here. Further discussion of this point can be found in Sects. 4.2 and 6 in Ch24.

For the purpose of this work, we assumed a power-law SN Ia DTD ($f_{Ia} \propto t^{-\alpha_{Ia}}$ at t> $\tau_{Ia;min}$ and zero at t< $\tau_{Ia;min}$) with $\alpha_{Ia} = 1$. This particular choice does not affect our conclusions (other f_{Ia} parametrisations are possible, but they degenerate into [O/Fe]-sSFR relations; see examples in Ch24). What is important, however, is the uncertain turning point of the relation, which for the assumed DTD is set by the minimum SN Ia delay $\tau_{Ia;min}$ (thin vertical lines in Fig. 2). Therefore, we define two variations:

(i) 'fast' Fe enrichment: $\tau_{Ia;min}$=40 Myr and m_{Fe}^{CCSN}=0.03 $M_{\odot}$ (or $C_{Ia/CC}$=2.5);
(ii) 'slow' Fe enrichment: $\tau_{Ia;min}$=400 Myr and m_{Fe}^{CCSN}=0.1 $M_{\odot}$ (or $C_{Ia/CC}$=0.74).

These choices can be considered extreme based on current theoretical expectations (see Sect. 5 in Ch24 and references therein). Until tighter constraints are available, we use variations (i) and (ii) to bracket the uncertainty in the [O/Fe]–sSFR relation. Additionally, we considered the following intermediate scenario.

(iii) 'Mixed' Fe enrichment: f_{Ia} from Kashino et al. (2022) and m_{Fe}^{CCSN}=0.05 $M_{\odot}$ (or $C_{Ia/CC}$=1.48)
where the f_{Ia} is based on an analytic theoretical model from Greggio (2005, 2010). This model accounts for a mixed contribution of different proposed SN Ia progenitors.

2.2. $Z_{O/H}$ at high z: Our model in light of JWST

The high $z > 3$ regime has only recently become accessible to empirical $Z_{O/H}$ studies, with the launch of JWST enabling the detection of the emission lines conventionally used to determine the gas–phase metallicity. Here, we took advantage of these new constraints to update our framework and validate assumptions about the $Z_{O/H}$ evolution made in ChN19 (i.e. an MZR with a strong z dependence) and Ch21 (an z-invariant FMR) . These two approaches give consistent $f_{SFR}(Z_{O/H}, z)$ up to $z \lesssim$3 but result in vastly different outcomes at higher z (Boco et al. 2021,Ch21).

We modelled the evolution of the MZR assuming that the FMR is z-invariant and compare it with the recent $z > 3$ observational samples (Nakajima et al. 2023; Curti et al. 2024; Chemerynska et al. 2024) in Fig. 3. We followed the phenomenological description of the FMR developed in Ch21, where the FMR is determined by the local MZR($z = 0$) and SFMR($z = 0$) relations and a single parameter ∇_{FMR0}. This approach captures the systematic differences in the FMR introduced by $Z_{O/H}$ and SFR determination methods (e.g. Kewley & Ellison 2008; Yates et al. 2012; Kashino et al. 2016; Telford et al. 2016; Maiolino & Mannucci 2019). The MZR(z) shown in Fig. 3 as solid lines correspond to maximum density regions occupied by our model galaxies in the $Z_{O/H}$ - $\log_{10}(M_*)$ plane at fixed z. This locus changes with z due to evolution of both SFMR and GSMF. We assumed the MZR($z = 0$) from Curti et al. (2020) (solid yellow line), SMFR, and GSMF as described in Sect. 2 [3].

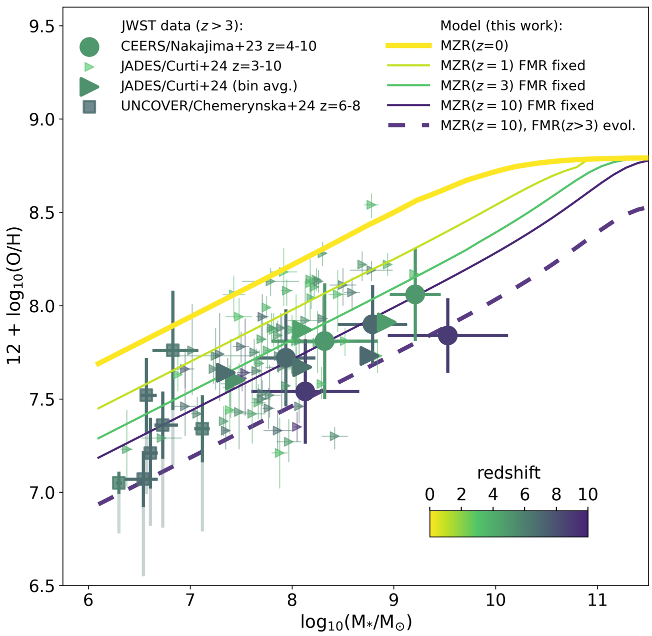

Fig. 3. Evolution of the gas-phase $Z_{O/H}$-MZR in our model against $z > 3$ data. The MZR(z>3), predicted based on the known evolution of the SFMR and z-invariant FMR (modelled as in Ch21), is consistent with current data; however, additional evolution may be present. The solid lines indicate the MZR at z=0, 1,3 10, assuming a z-invariant FMR. The dashed line indicates the MZR at z=10, assuming additional evolution in the FMR normalisation at $z > 3$. The data points represent the $z > 3$ samples from Nakajima et al. (2023) (circles, z-bin averages), Curti et al. (2024) (triangles: small for individual measurements, large for z-bin averages) and Chemerynska et al. (2024) (squares, assuming the calibration from Nakajima et al. (2022); the faint errors extend to the values estimated using the Sanders et al. (2024) calibration). The data points are coloured by redshift. This is shown for a variation described in Sect. 2 but using the MZR(z=0) from Curti et al. (2020) (i.e. without the +0.2 dex offset, to enable comparison with the reported data).

[2] Our results in terms of $Z_{Fe/H}$ and O/Fe values can simply be shifted by a constant to match alternative choices.

[3] MZR evolution is similar for all variations considered here, but see Ch21 and Fig. A4 therein for dependence on the MZR(z=0) and ∇_{FMR0}.

The resulting MZR shows a strong evolution up to $z \approx 1.5$ (in the last ≈9.5 Gyr), by which point the average $Z_{O/H}$ of $\log(M_*/M_\odot) \lesssim 9$ galaxies decreases by ≈0.3 dex. This is broadly consistent with the observational estimates, showing that the average $Z_{O/H}$ of galaxies at $z \approx$ 1–3 are lower than estimated from $z = 0$ MZR by about 0.3 dex (e.g. Sanders et al. 2021; Topping et al. 2020; Cullen et al. 2021; Henry et al. 2021; Revalski et al. 2024; Stanton et al. 2024). The evolution within the z = 1–3 range is difficult to quantify empirically as it is comparable to measurement uncertainties (e.g. Henry et al. 2021) and smaller than the systematics (e.g. Laseter et al. 2024; Stanton et al. 2024) introduced by different high-z strong-line metallicity calibrations used in the literature (e.g. Bian et al. 2018; Curti et al. 2020; Nakajima et al. 2023; Sanders et al. 2024).

At $z > 3$, the MZR in our universal FMR model decreases further by ≈0.2 dex by $z \approx 6$ and shows little evolution beyond this point. Observationally, the exact evolution of the MZR between z = 3–10 is currently unclear. Curti et al. (2024) analysed a sample of z =3-10 galaxies from the JADES (Bunker et al. 2023) and CEERS (Finkelstein et al. 2023) surveys, finding an ∼0.05 dex – 0.25 dex offset with respect to z∼3 MZR (depending on the reference z = 3 relation). This is consistent with Nakajima et al. (2023), who report lower average $Z_{O/H}$ in their z = 8–10 bin but consistent with no MZR evolution between z = 4–10 within errors. Both Nakajima et al. (2023) and Curti et al. (2024) find weaker $Z_{O/H}$ evolution at the low M_* end. However, this has been challenged by Chemerynska et al. (2024), who analysed the low M_* galaxy sample from the UNCOVER survey (Bezanson et al. 2024).

The picture emerging from the current observations is that the normalisation of the MZR at z = 3–10 lies ≈0.4-0.7 dex below that of the $z = 0$ relation (Curti et al. 2024; Nakajima et al. 2023; Morishita et al. 2024). Even with this uncertainty, it is clear that the extrapolation used in ChN19, resulting in the >1 dex decrease in $Z_{O/H}$ between z = 3 and z = 10, severely underestimates galaxy $Z_{O/H}$ at high z. In turn, the z-invariant FMR from Ch21 to MZR(z) is broadly consistent with the current observational estimates up to z = 10. However, stronger evolution is also permitted within the current uncertainties (i.e. the universal FMR may result in overestimated $Z_{O/H}$ at $z > 6$). To account for this possibility, we introduced a variation of our model in which the FMR normalisation decreases by 0.25 dex between z = 3 and z = 10. For simplicity, we assumed that this decrease is linear with z (see Table B.1). The resulting MZR(z = 10) is shown in Fig. 3 as a dashed line.

3. Iron-dependent cosmic star formation history

3.1. Example variation

Here, we begin discussing our results by highlighting the key differences between iron- and oxygen-based metallicity-dependent cSFH. Figure 4 shows the $f_{\rm SFR}(Z_{Fe/H}, z)$ (plotted as a 2D histogram in the [Fe/H] - z plane, coloured by the SFRD) for our example variation described in Sect. 2. The corresponding $f_{\rm SFR}(Z_{O/H}, z)$ is shown in Fig. F.1. To compare the iron- and oxygen-based results, we plot the SFRD-weighted averages of [Fe/H] and [O/H] at each z (solid lines: $\langle$[Fe/H]$\rangle_{\rm SFRD}$ in brown; $\langle$[O/H]$\rangle_{\rm SFRD}$ in black). We note the following observations.

(i) The SFRD-weighted average metallicity is lower when iron is used as a metallicity probe instead of the oxygen, reflecting the delay in iron enrichment relative to oxygen. Similarly, the distribution $f_{\rm SFR}(Z_{Fe/H}, z)$ extends to lower metallicities than $f_{\rm SFR}(Z_{O/H}, z)$. In Sect. 4 we show that their offset is sensitive primarily to the [O/Fe]−sSFR relation.

(ii) The offset between the $\langle$[Fe/H]$\rangle_{\rm SFRD}$ and $\langle$[O/H]$\rangle_{\rm SFRD}$ increases with z until $z \approx 3$, where $\langle$[Fe/H]$\rangle_{\rm SFRD}$ shows a steeper evolution. At $z > 3$ this offset approaches a constant value. This is a consequence of the weak evolution of galaxy sSFRs at $z \gtrsim 3$ and, thus, their locations on the [O/Fe]−sSFR plane.

(iii) The mismatch between the two distributions suggests that the star formation with a solar O/Fe abundance ratio is rare throughout cosmic history (see Fig. F.2, showing the corresponding [O/Fe]-dependent cosmic SFH).

We further discuss quantifying point (iii) in Sect. 4.

3.2. Cross-check with observational samples

While the $f_{\rm SFR}(Z_{O/H}, z)$ was obtained by combining the empirical properties of galaxy populations across z, the $f_{\rm SFR}(Z_{Fe/H}, z)$ was inferred more indirectly. The $Z_{\rm Fe/H}$ of young stars or gas was estimated from the galaxy's $Z_{\rm O/H}$ and sSFR via the [O/Fe]–sSFR relation. To assess whether our results fall within a reasonable range, we compared them against three reference observational samples that probe different regions of $f_{\rm SFR}(Z_{\rm Fe/H}, z)$, as discussed below and shown in Fig. 4.

3.2.1. RR Lyrae: [Fe/H] in low-mass, high-z galaxies

RR Lyrae are pulsating stars with typical ages of $\gtrsim$ 10 Gyr, reaching $\gtrsim$ 12.5 Gyr in GCs and in the lowest-mass dwarf galaxies (Catelan 2004, 2009; Sesar et al. 2014). They trace the properties of the oldest stellar populations. Following Bellazzini et al. (2025), we adopted the mean metallicity of RR Lyrae stars in local dwarf galaxies ($\langle$[Fe/H]$\rangle_{\rm RRLyr}$) as a proxy for the iron enrichment of the lowest-mass galaxies ($M_* < 10^8\,M_\odot$) at $z \gtrsim$ 2–5 (look-back times $\gtrsim$10 - 12.5 Gyr). Specifically, we used the values listed in Table A.1 of Bellazzini et al. (2025), based on the [Fe/H] estimates from Muraveva et al. (2025). These were derived from the pulsation periods and Fourier decomposition parameters of RR Lyrae light curves in Gaia data release 3 (Clementini et al. 2023).

As a minimum requirement, any viable model must reproduce the formation of stars with $\langle$[Fe/H]$\rangle_{\rm RRLyr}$ at $z \gtrsim 2$ in the regime where galaxies with $M_* < 10^8\,M_\odot$ contribute to $f_{\rm SFR}(Z_{\rm Fe/H}, z)$. Figure 4 shows that this is the case and that the full extent of the low [Fe/H]–high z tail of the $f_{\rm SFR}(Z_{Fe/H}, z)$ probed by RR Lyrae can only be populated by star formation in $M_* < 10^8 M_\odot$ galaxies. Conversely, not accounting for such galaxies results in negligible star formation at [Fe/H]<-2 at any z covered by our models.

3.2.2. MW globular clusters: [Fe/H] at high SFRD

Globular clusters are old stellar systems, each thought to have formed during a brief star formation episode. While they host multiple stellar populations distinguished by variations in their light-element abundances, they generally exhibit only small spreads in $Z_{\rm Fe/H}$, likely reflecting the iron content of the interstellar medium at the time of their formation (McKenzie & Bekki 2021; Legnardi et al. 2022; Monty et al. 2023; Legnardi et al. 2024). Both observations (e.g. Adamo et al. 2020a,b) and theory (e.g. Grudić et al. 2021) indicate that GC progenitor formation efficiency depends on the star-forming environment. Dense

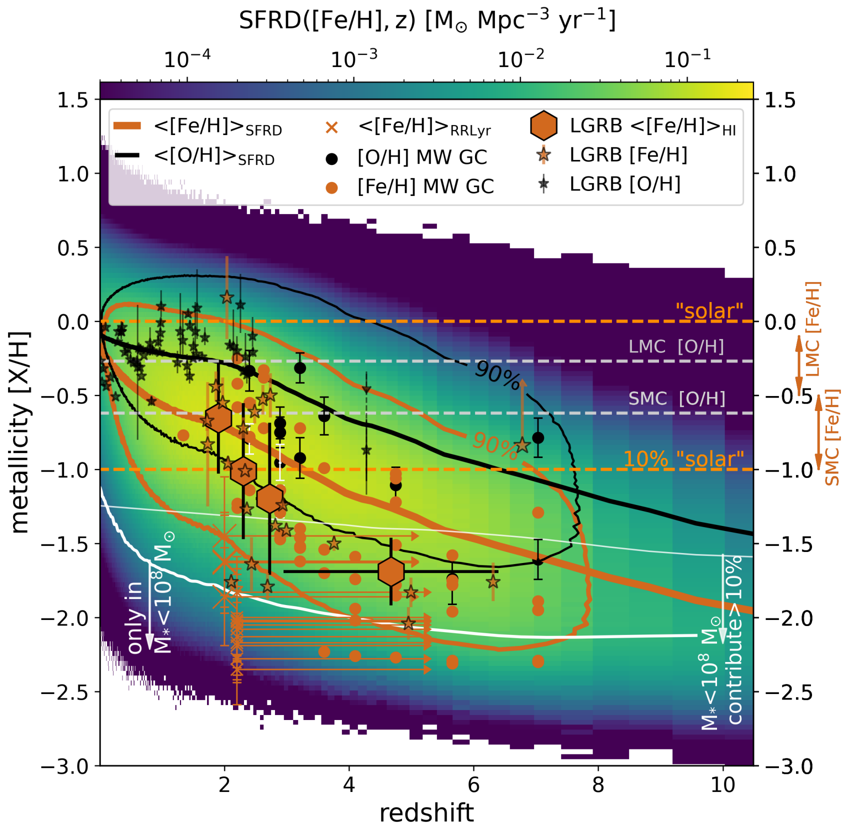

Fig. 4. Distribution of the cosmic SFRD at different [Fe/H] and z (colour scale), shown for an example variation described in Sect. 2. The black and brown lines indicate the SFRD-weighted average [O/H] and [Fe/H], respectively, at each z. The black and brown contours enclose 90% of the SFRD to further show the offset between the $f_{\rm SFR}$([O/H],z) and $f_{\rm SFR}$([Fe/H],z). The solid white lines show the [Fe/H] values below which $M_* < 10^8 M_\odot$ galaxies contribute at least 10% of the SFRD (thin line) and below which the contribution of $M_* > 10^8 M_\odot$ galaxies is negligible (thick line). The data points represent the cross-check samples introduced in Sect. 3.2. The hexagons represent the $\langle$[Fe/H]$\rangle_{\rm HI}$ values of the LGRB hosts binned in z. The brown and black stars present the [Fe/H] and [O/H] values of the individual LGRB hosts. The crosses indicate the mean [Fe/H] values of the RR Lyrae stars in local dwarf galaxies (small: $M_* < 10^8 M_\odot$, big: $M_* \gtrsim 10^8 M_\odot$, offset for visibility) but formed at $z > 2-5$ (horizontal arrows). The brown and black dots represent the [O/H] and [Fe/H] values of MW GCs. [O/H] and [Fe/H] values for the LMC and SMC on our solar scale are indicated for the reference.

and most actively star-forming regions (such as those found in local starbursts or in the early Universe) favour the formation of massive, long-lived clusters that can evolve into today's GCs (Adamo et al. 2020b; Reina-Campos et al. 2022; Kruijssen 2025). Thus, we expect GCs to preferentially probe the regions of $f_{\rm SFR}(Z_{\rm Fe/H}, z)$ with high-SFRDs and, due to the FMR, low $Z_{\rm Fe/H}$, while avoiding the extremes of the distribution.

In Fig. 4, we plot the sample of MW GCs with isochronal ages and $Z_{\rm Fe/H}$ from VandenBerg et al. (2013). For each cluster, we assumed its best-fit age corresponds to the look-back time/z of its formation. We also show $Z_{\rm O/H}$ measurements for 16 MW GCs from Carretta et al. (2009), noting that GC stars can display large internal spreads in this element. We adopted the $Z_{\rm O/H}$ values from Monty et al. (2025) (shifted to our solar scale), who restricted their analysis to O-normal populations and applied a +0.15 dex correction to place the estimates on a common abundance scale with other MW samples (namely the GALAH survey Buder et al. 2021), using Amarsi et al. (2019) as a baseline for their detailed treatment of non-local thermodynamic equilibrium effects.

Figure 4 shows that most of the MW GCs ($Z_{\rm Fe/H}$: brown dots; $Z_{\rm O/H}$: black dots) fall within the corresponding $f_{\rm SFR}(Z_{\rm Fe/H}, z)$ and $f_{\rm SFR}(Z_{\rm O/H}, z)$ contours, which enclose the regions where the bulk of stellar mass formed. As expected, none of the GCs are found in the extreme tail of the distribution (dark blue area). However, a few GCs [4] fall in the region where, according to our model, star formation occurs almost exclusively in galaxies with $M_* < 10^8\,M_\odot$. This is somewhat surprising, as such low-mass systems are generally not considered capable of (efficiently or at all) forming the massive (initially $\gtrsim 10^6\,M_\odot$) star clusters that are the progenitors of present-day GCs (Renaud 2018; Krumholz et al. 2019; Adamo et al. 2020b). Interestingly, all of the GCs which fall in this region have been tagged as accreted clusters based on their orbits, chemistry of their O-normal population, or a combination of both orbits and chemistry (Massari et al. 2019; Massari 2025; Belokurov & Kravtsov 2024; Monty et al. 2024). A more detailed discussion is beyond the scope of this paper, but we aim to return to this comparison in a follow-up study.

[4] NGC4590, NGC5053, NGC5466, NGC6341, NGC7078, NGC7099, and Terzan 8

3.2.3. Long gamma-ray burst hosts: (Lower limit on the) $\langle$[Fe/H]$\rangle_{\rm SFRD}(z)$

Long-duration gamma-ray bursts are typically linked to the deaths of massive stars and are found in actively star-forming regions (e.g. Galama et al. 1998; Hjorth et al. 2003; Christensen et al. 2004; Fruchter et al. 2006). They are among the most energetic electromagnetic transients known and have been detected out to $z \gtrsim 8$ (Tanvir et al. 2009), probing star-forming environments across cosmic time. Long-duration gamma-ray burst afterglows allow to determine the gas-phase $Z_{\rm Fe/H}$ in their hosts via absorption-line spectroscopy (e.g. Vreeswijk et al. 2004). This is especially valuable for our study, since direct constraints on $Z_{\rm Fe/H}$ in high-z star-forming environments are scarce. Furthermore, unlike galaxies selected in conventional surveys, LGRB-afterglow-selected systems are not expected to be biased against faint objects.

We used the absorption-derived LGRB host properties (total metallicity - $[M/H]_{\rm tot}$, z, and HI column density - $N_{\rm HI}$) compiled by Heintz et al. (2023), covering $1.7 < z < 6.3$. We also included GRB 050505 at $z \approx 4.28$ (Berger et al. 2006, as reanalysed by Inkenhaag et al. 2025), and GRB 240218A at $z \approx 6.78$, for which only the lower limit of $[M/H]_{\rm tot} \geq -0.8$ is available

(Saccardi et al. 2025, revised analysis). Importantly, $[M/H]_{\rm tot}$ represents the total metallicity (gas plus dust) of the interstellar medium (ISM), corrected for dust depletion (e.g. De Cia et al. 2016, 2018). This correction is critical for iron, which is strongly depleted into dust grains (by 90-99% in the MW; e.g. Jenkins 2009, and up to 90% in lower-metallicity environments; e.g. De Cia et al. 2016; Konstantopoulou et al. 2024). The $[M/H]_{\rm tot}$ value is equivalent to a dust-corrected [Fe/H] when Zn abundance is available to guide the dust correction. If this is not the case, S or Si can be used for dust corrections. However, such estimates are more approximate, and the resulting $[M/H]_{\rm tot}$ may overestimate $Z_{\rm Fe/H}$ unless α-enhancement is explicitly accounted for (Saccardi et al. 2023; De Cia et al. 2024). We assumed that the $[M/H]_{\rm tot}$ values obtained with Zn-based dust corrections (i.e. GRB 240218A as well as 21 of the 36 objects from Heintz et al. 2023) provide a reliable proxy for $Z_{\rm Fe/H}$. We also assumed that this is the case for GRB 210905A, as its $[M/H]_{\rm tot}$ accounts for α-enhancement (Saccardi et al. 2023).

We plot the [Fe/H] estimates for individual LGRB hosts in this sample in Fig. 4, and we use those estimates (without the lower limit from GRB 240218A) to re-derive the $N_{\rm HI}$-weighted mean $\langle$[Fe/H]$\rangle_{\rm HI}$ with z, following Eq. 2 of Heintz et al. (2023) (see Table D.1 in the appendix for the binning and values). In Sect. 6 we also show the $\langle$[M/H]$\rangle_{\rm HI}$ values obtained for the full sample. Weighting by $N_{\rm HI}$ accounts for the varying amounts of potentially star-forming gas in the probed galaxies. This enables a comparison between $\langle$[Fe/H]$\rangle_{\rm HI}(z)$ and the $\langle$[Fe/H]$\rangle_{\rm SFRD}(z)$ derived from our models. However, the comparison is complicated by the fact LGRB progenitors are theorised to be massive, iron-poor stars (Hirschi et al. 2005; Yoon & Langer 2005; Woosley & Heger 2006, but see Chrimes et al. 2020; Briel et al. 2025). Thus, they may preferentially occur in regions of high star formation and low $Z_{\rm Fe/H}$. Empirical studies indicate a decline in LGRB occurrence rate near solar metallicity but overall find no clear cutoff or preference for extremely metal-poor environments (e.g. Vergani et al. 2015; Japelj et al. 2016; Perley et al. 2016; Graham et al. 2023; Disberg et al. 2025). Moreover, at intermediate redshifts, LGRB host galaxies appear to trace the star-forming population (Krogager et al. 2024, selected by having cold gas and active starformation). In the presence of such biases, the LGRB-based $\langle$[Fe/H]$\rangle_{\rm HI}$ provides a lower limit on the overall $\langle$[Fe/H]$\rangle_{\rm SFRD}$, and we expect the offset between the two to decrease towards high z, where galaxies have higher SFRs and lower $Z_{\rm Fe/H}$.

Finally, while we focus on $Z_{\rm Fe/H}$, in Fig. 4 we also show $z \lesssim 2.5$ LGRB hosts with emission-line $Z_{\rm O/H}$ estimates from Graham et al. (2023) (obtained with Curti et al. 2017, 2020 calibration, shifted by +0.2 dex for consistency with our scale) and GRB 050505 (Inkenhaag et al. 2025), for which we show the range of $Z_{\rm O/H}$ obtained with different methods. We note that samples with emission-line based $Z_{\rm O/H}$ are subject to the usual selection effects, favouring brighter (more massive, lower redshift) sources. We refer the interested reader to Disberg et al. (2025) for a recent detailed discussion of the comparison with this sample.

Based on the comparison shown in Fig. 4 we note the following:

- The $Z_{\rm Fe/H}$ and $Z_{\rm O/H}$ of individual LGRB hosts show appreciable scatter, which our model fully accounts for.
- The $\langle$[Fe/H]$\rangle_{\rm HI}$ from absorption-derived LGRB host properties does not trace $\langle$[O/H]$\rangle_{\rm SFRD}$. However, $\langle$[Fe/H]$\rangle_{\rm SFRD}$ is broadly consistent with $\langle$[Fe/H]$\rangle_{\rm HI}$.

This second point demonstrates the importance of accounting for non-solar abundance ratios when comparing 'metallicities' probed by different elements, particularly in the context of the potential low metallicity bias of LGRB. Our model predicts a milder evolution than the LGRB-based estimate in the highest-z bin; however, the $\langle$[Fe/H]$\rangle_{\rm HI}$ estimate in this bin is likely unreliable (see Sect. 6, where we also compare across model variations), and we refrain from drawing conclusions from comparisons in this z range.

4. How (un)common is the solar abundance pattern?

4.1. The oxygen-to-iron abundance ratio over cosmic time

The example discussed in Sect. 3 shows a persistent offset between $\langle$[O/H]$\rangle_{\rm SFRD}$ and $\langle$[Fe/H]$\rangle_{\rm SFRD}$, i.e. the SFRD-weighted mean $\langle$[O/Fe]$\rangle_{\rm SFRD} > 0$ at all redshifts. This indicates that most of the cosmic star formation happened with O/Fe ratio larger than 'solar'. We quantify this result and its sensitivity to assumptions about the uncertain factors in our model in Fig. 5.

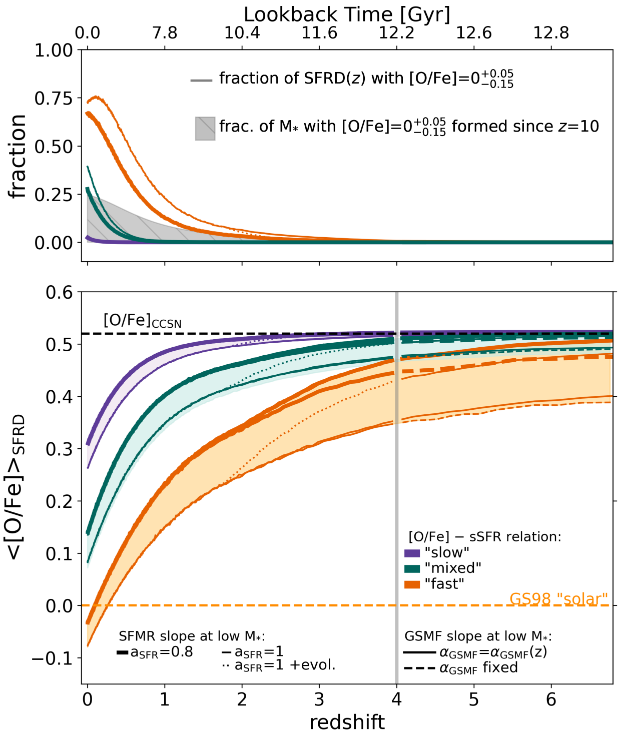

Fig. 5. Top: Fraction of cosmic stellar mass (grey-shaded area) formed since z=10 with near-solar [O/Fe] (between –0.15 and 0.05 dex). Across our models, this fraction is at most 25%. The lines indicate the fraction of the total SFRD(z) formed with near-solar [O/Fe]. Bottom: SFRD weighted mean [O/Fe] as a function of redshift. At $z < 4$ ($z > 4$), the line styles distinguish between the assumptions for the SFMR ($\alpha_{\rm GSMF}$). The colours indicate the [O/Fe]–sSFR relation, and the coloured areas indicate the range spanned by models with a fixed [O/Fe]–sSFR relation. The dotted green line represents our example variation.

The [O/Fe]–sSFR relation represents the dominant source of uncertainty in the $\langle$[O/Fe]$\rangle_{\rm SFRD}$ and in the fraction of the SFRD with 'near-solar' O/Fe abundance ratios, liberally defined here as a range between [O/Fe]=-0.15 and 0.05 dex ($\log_{10}$(O/Fe)=1.18 - 1.38) to enclose the different reference solar abundance ratios used in the literature [5]. The colours in Fig. 5 correspond to differ-

[5] $Z_{\rm Fe/H}$ = 7.45 - 7.5 and $Z_{\rm O/H}$=8.69 - 8.83 (Lodders et al. 2009; Asplund et al. 2009, 2021; Grevesse & Sauval 1998), yielding -0.15 to +0.05 offsets in [O/Fe] relative to our scale.

ent average [O/Fe]–sSFR relations, varied between the extreme cases discussed in Sect. 2.1. The $\langle[\mathrm{O/Fe}]\rangle_{\mathrm{SFRD}}$ approaches the solar value only in the 'fast' Fe-enrichment scenario (orange curves), which assumes the minimum possible delay between CCSN and the onset of enhanced Fe enrichment. Even in this case, $\langle[\mathrm{O/Fe}]\rangle_{\mathrm{SFRD}} \lesssim 0$ only at $z \lesssim 0.4$. At the other extreme, using the [O/Fe]–sSFR relation corresponding to the 'slow' Fe-enrichment scenario (purple curves) yields $\langle[\mathrm{O/Fe}]\rangle_{\mathrm{SFRD}} \gtrsim 0.25$ dex even at z=0. In this case, the fraction of SFRD($z = 0$) with 'near-solar' O/Fe ratio is $\lesssim 2\%$. We note that the fraction of cosmic stellar mass formed with near-solar [O/Fe] is the most sensitive to the [O/Fe]–sSFR relation around $\log_{10}(\mathrm{sSFR}) \sim -9$ (i.e. main-sequence galaxies at $z \sim 0.6$–2). Only a steeper drop to solar-like [O/Fe] in this regime can visibly increase this fraction. However, a relation steeper in this regime than our extreme 'fast' Fe-enrichment scenario would challenge the current constraints on the relation (see Fig. 2 and Ch24). Variations in the shape of the relation at lower sSFR only have a marginal impact, because such galaxies contribute little to the (integrated) cosmic SFRD budget.

Another important factor for these results is the distribution of galaxy sSFRs: a higher fraction of galaxies with a high sSFR increases $\langle[\mathrm{O/Fe}]\rangle_{\mathrm{SFRD}}$, whereas weaker evolution in galaxy sSFR with z leads to weaker evolution of $\langle[\mathrm{O/Fe}]\rangle_{\mathrm{SFRD}}$. To quantify this effect, we consider in Fig. 5 three variations of the SFMR (shown in Fig. 1): the relation from P23 (thin solid lines), the same relation but with a shallower slope (a_{SFR}=0.8 instead of a_{SFR}=1 at low M_*; thick solid lines), and a version with increased high-z evolution (dotted lines; as in the example in Sect. 3). We varied a_{SFR} because (i) our analysis extends to galaxies with M_* much lower than the $\log_{10}(\mathrm{M}_*/\mathrm{M}_\odot)$>8.7 value adopted in P23 to restrict their fit to regimes with high sample completeness and because (ii) a_{SFR} has a strong impact on our results. Adopting a_{SFR}=0.8 instead of a_{SFR}=1 results in ~1 dex higher $\log_{10}(\mathrm{SFR})$ at $M_* = 10^6 M_\odot$. While observational studies report even lower a_{SFR} values (particularly at high z; see e.g. compilations in Speagle et al. 2014; Boogaard et al. 2018; Mérida et al. 2023), Simmonds et al. (2025) attribute these to sample incompleteness, while Leja et al. (2015) argue that such shallow slopes are inconsistent with the observed evolution of the GSMF (see also Di Cesare et al. 2026). Moreover, assuming a_{SFR}<0.8 would cause a significant overestimate of the cSFH (see Sect. 5.1). The effect of a_{SFR} and/or galaxy sSFR evolution on $\langle[\mathrm{O/Fe}]\rangle_{\mathrm{SFRD}}$ can be partially offset by the abundance of low-M_* galaxies. In our framework, the latter is tied to uncertain low-M_* slope of the GSMF. Assuming a fixed α_{GSMF} (dashed lines at $z > 4$) versus $\alpha_{\mathrm{GSMF}}(z)$, which steepens with z, has a relatively small effect on the results shown in Fig. 5. Finally, we note that

– the fraction of mass formed in stars until the present day with [O/Fe] between −0.15 dex and 0.05 dex is at most 25% (grey band; see top panel in Fig. 5);
– the fraction of cosmic SFRD occurring with 'near-solar' [O/Fe] is negligible at $z > 2$ across our models. This fraction is negligible even at z ~0 if the delay between the CCSN enrichment and enhanced Fe production is long (O(10^8yr)).

The exact values shown in the top panel of Fig. 5 depend to some extent on the assumed metallicity scatter within galaxies. We discuss this further in Appendix C, where we derive a more conservative upper bound of $\lesssim$ 30% for the fraction of stellar mass formed with near-solar [O/Fe], adopting the extreme assumption that the stellar $Z_{\mathrm{Fe/H}}$ and $Z_{\mathrm{O/H}}$ distributions within a host are fully independent. We therefore conclude that the specific treatment of scatter does not affect our main result that star formation with near-solar [O/Fe] is rare. This starkly contrasts with the fact that most stellar evolution and spectral synthesis models used in the literature and applied to interpret observations – including those of young and high-z environments – assume a solar abundance pattern (in particular, [O/H] ≈ [Fe/H] ≈ $\log_{10}(Z/Z_\odot)$). We discuss the implications of this result in Sect. 7.

4.2. The relevance of the solar abundance pattern

In this section, we argue that the results presented above are broadly consistent with (i) the MW being representative of the star-forming galaxy population at the solar formation epoch (~4-5 Gyr ago or $z \approx 0.4$), i.e. that a galaxy with MW-like properties is a typical draw from the distributions introduced in Sect. 2, and with (ii) the Sun's abundances being common among stars formed in such systems at that time.

First, we verified that in our model, MW-like galaxies (i.e. galaxies with masses of $\log_{10}(M_*/M_\odot) \approx 10.4 - 10.5$ at $z = 0.4$ and $\log_{10}(M_*/M_\odot) \approx 9.9 - 10$ at $z = 2$ (e.g. Patel et al. 2013; Grand et al. 2017) are among the dominant contributors to the cosmic SFRD at $z \lesssim 2$, consistent with the picture that the MW and its progenitors are representative L_* systems. This contribution was computed by weighting the SFR of main-sequence galaxies of different masses by their number density n_{gal} (given by the GSMF). The result is shown in Fig. 6 at several redshifts, with the thick dashed curve indicating the epoch of solar formation ($z = 0.4$). We find a relatively broad range in $\log_{10}(M_*)$ contributing comparably to the cosmic SFRD, with the main-

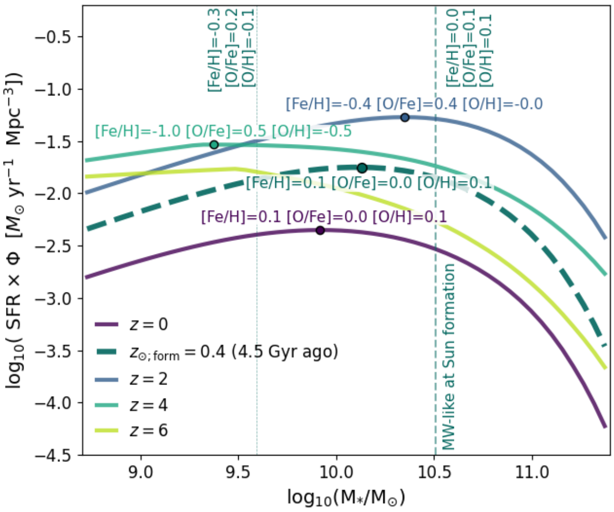

Fig. 6. Contribution to the cosmic SFRD (SFR density per log M_* bin) vs galaxy $\log_{10}(\mathrm{M}_*)$ at several redshifts (colour-coded; bottom and top curves correspond to z=0 and z=2, respectively, illustrating the evolution of the cSFH). The filled circles mark the $\log_{10}(\mathrm{M}_*)$ at which the contribution peaks at each z (ill-defined for z >4). At each marked mass, we list the typical abundances ([O/Fe],[O/H], and [Fe/H]) of the star-forming gas in our model. The thick dashed curve highlights $z \approx 0.4$, corresponding to a look-back time of 4.5 Gyr (the epoch of solar birth). The vertical dashed lines show $\log_{10}(\mathrm{M}_*)$ within ±0.1 dex of the $z = 0.4$ peak; the abundances for these two masses are reported at the top. This mass range encompasses main-sequence galaxies with stellar masses comparable to that of the MW at the epoch of solar formation (i.e. not its present-day mass), which were forming stars with near-solar abundance ratios. This is shown for our example variation.

sequence galaxies with masses comparable to that of the MW at the epoch of solar formation lying within ±0.1 dex of the peak (between the vertical dashed lines in Fig. 6).

Second, we examined the gas-phase abundances assigned to such galaxies at a look-back time of 4–5 Gyr in our model. These are reported in the top-right corner of Fig. 6 for our example variation. Using the FMR, we find [O/H] ≈ 0.1 dex. Taken at face value, this would make the Sun ([O/H] = 0) appear mildly O-poor relative to the average abundances of stars formed at that epoch in MW–like galaxies (adopting a different $Z_{O/H,\odot}$ than our reference value from Grevesse & Sauval (1998) would generally increase this offset). However, a ∼ 0.1 dex offset in $Z_{O/H}$ is comparable to the intrinsic scatter of the MZR ($\sigma_{\rm MZR} \approx 0.1$ dex at high M_*), implying that MW-like galaxies with [O/H] = 0 lie within the typical population at $z = 0.4$. Moreover, given the Sun's galactocentric distance of $\gtrsim 1.5, R_e$ and the negative $Z_{\rm O/H}$ gradients commonly observed in spirals, it may have formed at a lower $Z_{\rm O/H}$ than the global value inferred from galaxy scaling relations (assumed to be representative of the average at R_e). Ch24 estimate a possible ∼ −0.05 dex offset due to the MW gradient (Arellano-Córdova et al. 2020), comparable to the abundance spread observed among solar-like (i.e. similar in age and [Fe/H]) disk stars (Nissen 2015).

The corresponding [O/Fe] for a main-sequence galaxy with MW–like mass at $z = 0.4$ follows from the [O/Fe]–sSFR relation, and [Fe/H] = [O/H] − [O/Fe]. In our 'mixed' Fe-enrichment scenario (assumed in Fig. 6), this yields [O/Fe] = 0.1 dex and [Fe/H] = 0. Adopting alternative relations leaves [O/H] unchanged but shifts both [Fe/H] and [O/Fe] by ±0.2 dex, making the Sun appear either Fe-poor ('fast' enrichment) or Fe-rich ('slow' enrichment) relative to the average abundances of its host galaxy at the solar formation epoch. The intrinsic scatter in the $Z_{\rm Fe/H}$–MZR for MW–mass galaxies, as well as the MW's radial gradient, is comparable to those for $Z_{\rm O/H}$ (e.g. Gallazzi et al. 2005; Spina et al. 2021), implying an expected ∼ 0.1 dex spread in average $Z_{\rm Fe/H}$ across the galaxy population. Within galaxies, the dispersion of the $Z_{\rm Fe/H}$ metallicity distribution function (MDF) for solar-neighbourhood thin-disk stars at fixed age is ∼ 0.15–0.2 dex (Casagrande et al. 2011; Hayden et al. 2015; Buder et al. 2021; Feuillet et al. 2019). Thus, even if the mean [Fe/H] of MW–like galaxies at $z = 0.4$ differs by ±0.2 dex, stars with solar [Fe/H] are still expected to form given the observed internal scatter.

In principle, all our model variations predict the formation of stars with solar abundance ratios in MW-like galaxies at the solar formation epoch, within the expected scatter. However, such stars need not align with the peak of the MDF in MW-like galaxies. The match is closest for an [O/Fe]–sSFR relation intermediate between our 'mixed' and 'fast' Fe-enrichment scenarios, and poorest if the relation resembles the 'slow' Fe-enrichment case. In the latter case, negative radial metallicity gradients would further exacerbate deviations from solar $Z_{\rm Fe/H}$ and $Z_{\rm O/H}$. Zooming out to the cosmic volume, depending on the [O/Fe]–sSFR relation, stars with [O/Fe]=0 at the solar formation epoch would either coincide with the peak of the [O/Fe] distribution ('fast', Fig. F.3), lie within the region enclosing 95% of the cosmic SFRD ('mixed', Fig. F.2), or fall outside the contours enclosing 99% of the cosmic SFRD ('slow'). A detailed comparison of our work with the MW requires careful accounting for selection effects, completeness, and systematics in MW stellar surveys, as well as a more careful treatment of the metallicity spread within the galaxies in our model, which is beyond the scope of this paper. For the purposes of this discussion, we note that if the MW is representative of star-forming galaxies and if the near-solar $Z_{\rm O/H}$ and $Z_{\rm Fe/H}$ values are typical of stars formed in such systems at $z \lesssim 0.4$, then our 'slow' Fe-enrichment scenario is disfavoured.

5. Cosmic star formation history: Model variations

5.1. Total cosmic star formation history

Figure 7 shows the cSFH obtained under different combinations of assumptions in our model together with literature observational estimates. This serves as an important consistency check: although our framework is based on empirical relations, it does not include any normalisation to match independent constraints on the cSFH when these relations are combined. The observational data shown include UV-based estimates (blue data points) compiled by Madau & Dickinson (2014), together with the recent $z > 6$ estimates from Rinaldi et al. (2022) (with the lower limit based on the galaxies in the COSMOS/SMUVS catalogue), Donnan et al. (2024), Whitler et al. (2025), and Chemerynska et al. (2024) (with all three based on the integration of the UV luminosity functions to the same limiting magnitude $M_{UV} = -17$). Additionally, we show the IR/(sub)millimetre-based estimates (red data points and limits) compiled by Casey et al. (2018), together with the estimates from Gruppioni et al. (2020), Loiacono et al. (2021), Khusanova et al. (2021), and Algera et al. (2023). These studies sample the contribution of dusty star-forming galaxies, constraining the obscured fraction of the SFRD to z ∼7. Martis et al. (2025) probed the obscured fraction with photometry up to $z = 9$, finding that up to ∼50% of all SFR may still be obscured at those early epochs. Consequently, this component could be missed by the UV luminosity function-based SFRD estimates.

As discussed in the previous section, we varied the contribution of low-M_* galaxies by changing $\alpha_{\rm GSMF}$ (top panel in Fig. 1) and $a_{\rm SFR}$ and considered increased $z \gtrsim 2$ evolution of the SFMR with respect to P23 (middle panel in Fig. 1). In grey we show the cSFH obtained assuming a high SB contribution (see Appendix A.6), motivated by the results of Caputi et al. (2017); Rinaldi et al. (2022, 2025), who find a SB fraction $f_{SB}(M_*, z)$ that strongly increases with z and towards low M_*.

A direct comparison of our results with estimates from the literature is complicated by methodological differences. In particular, a consistent treatment would require mapping the galaxy properties used in our model (SFR, M_*, and metallicity) and the observed galaxy luminosities, as well as homogenising assumptions regarding integration limits and extrapolations beyond sample completeness. Each of these aspects can introduce offsets by a factor of a few in the inferred SFRD, and their proper assessment lies beyond the scope of this work. We therefore adopted a conservative approach, not excluding any model variations that agree with literature SFRD estimates within a factor of 10. These estimates are particularly sensitive to the assumed lower limit of the integration, whether in M_* (our estimates) or in IR/UV luminosity (literature), where galaxy properties are uncertain. To illustrate this, we show in Fig. 7 (hatched regions) the effect of raising the lower integration limit from $M_{min} = 10^6 M_\odot$ to $M_{min} = 10^8 M_\odot$ for several variations. The impact grows with z, as does the apparent mismatch with literature estimates, reaching a factor between 3–5 at $z = 8$ for models with evolving $\alpha_{\rm GSMF}(z)$ and $a_{\rm SFR} = 0.8$ or with a high SB contribution (both elevate SFR at $M_* < 10^9 M_\odot$). By contrast, for $\alpha_{\rm GSMF}=\alpha_{\rm fix}$, the effect is negligible at $z \gtrsim 9$.

We note that a high SB contribution would overestimate the SFRD at $z > 2$ by a factor >10 compared to literature values, even for $M_{min} = 10^8 M_\odot$, unless $a_{\rm SFR} \gtrsim 1$ (which is not the case in

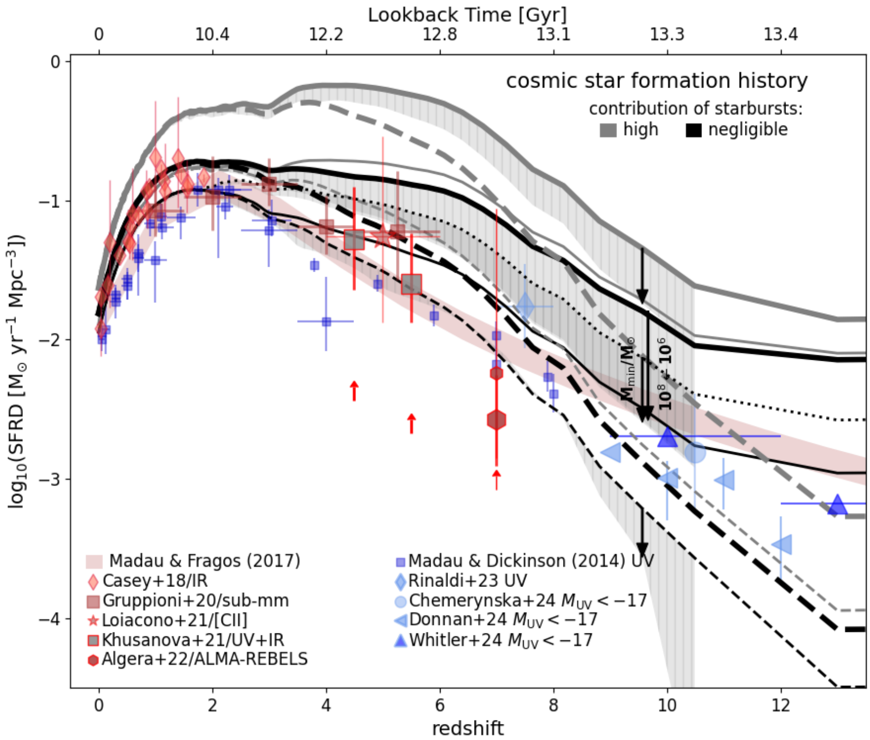

Fig. 7. cSFH for different combinations of assumptions on the GSMF (solid lines: $\alpha_{\rm GSMF}$ steepening with z, dashed lines: $\alpha_{\rm GSMF}$ fixed; see top panel in Fig. 1) and the SFMR (thin and thick lines: P23 with $a_{\rm SFR}$=1 and $a_{\rm SFR}$=0.8, respectively; dotted line: P23 with additional evolution at $z > 2$; see middle panel of Fig. 1). We also show the effect of different contributions of starbursts (black and grey lines for negligible and high, respectively). The data points indicate observational estimates (see legend). The red band indicates the estimate from Madau & Fragos (2017). Where necessary, we adjust the literature estimates to the Kroupa (2001) IMF assumed here. The hatched regions illustrate the effect of increasing the lower limit of the integration over galaxy stellar mass from $10^6 M_\odot$ to $10^8 M_\odot$. The dotted line shows the cSFH of the variation considered in Sect. 3.

Rinaldi et al. 2022, 2025). Such variations were not considered further. The limiting case with high f_{SB} and $a_{\rm SFR}$ = 1 (hereafter 'high f_{SB}') is, for our results, effectively indistinguishable from a scenario without an SB sequence but with $a_{\rm SFR}$ evolving with z ($a_{\rm SFR} \sim 0.9$ at $z = 0$ and $a_{\rm SFR} \lesssim 0.8$ at $z > 2$). The corresponding results are qualitatively similar to those for the $a_{\rm SFR}$ = 0.8 case and, for clarity, we do not show them in all figures. Finally, while our analysis does not extend beyond z >10.5, we show in Fig. 7 the cSFH up to $z \sim 13$ to highlight its strong dependence on the extrapolation of the GSMF (see Appendix A.5).

5.2. 'Low-metallicity' cosmic star formation history

The 'low-metallicity' cSFH (obtained by only considering cosmic SFRDs below a certain metallicity threshold) is where the differences between oxygen- and iron-based results are most pronounced. The dotted lines in the right panel of Fig. 8 illustrate this for the example variation discussed in Sect. 3 and compare the total (top line) and the 'low-metallicity' cSFH traced by either $Z_{\rm Fe/H}$ (middle line) or $Z_{\rm O/H}$ (bottom line). These were obtained by integrating $f_{\rm SFR}(Z_{\rm Fe/H}, z)$ and $f_{\rm SFR}(Z_{\rm O/H}, z)$ (shown in Figs. 4 and F.1) up to the same relative 'low-metallicity' threshold, [Fe/H] = [O/H] = –0.65, defined as the logarithm of the elemental abundance relative to solar. This threshold was chosen arbitrarily but roughly selects sub-Small Magellanic Cloud (SMC) metallicity environments[6]. For the example variation, nearly all SFRDs at $z \gtrsim 4$ occur below the SMC-like [Fe/H] and occur at $z \gtrsim 8$ if this threshold is defined in terms of oxygen abundance. The orange and blue regions shown in Fig. 8 span the cosmic SFRDs below [Fe/H] < –0.65 and [O/H] < –0.65, respectively, calculated across model variations and illustrating the associated uncertainties. While the quantitative outcome depends on the chosen metallicity threshold (with lower thresholds yielding larger uncertainties) the qualitative behaviour remains consistent with that described for the example variation. The overlap between the two ranges increases with z as the fraction of SFRD below the metallicity threshold approaches the total (grey area), occurring at lower z for iron- as opposed to oxygen-based cut. When compared to the same relative threshold, the SFRD is higher at a 'low' $Z_{\rm Fe/H}$ than at a 'low' $Z_{\rm O/H}$, and the low-$Z_{\rm Fe/H}$ cSFH peaks at a lower z than its oxygen counterpart.

At $z \lesssim 4$, the orange range is wider than the blue one due to the additional uncertainty introduced by the [O/Fe]−sSFR relation. As shown in Sect. 4, in the 'fast' Fe-enrichment scenario the difference between the $f_{\rm SFR}(Z_{Fe/H}, z)$ and the $f_{\rm SFR}(Z_{O/H}, z)$ (therefore, also between low-$Z_{\rm Fe/H}$ and low-$Z_{\rm O/H}$ cSFH) is the smallest. This difference is the largest in the 'slow' Fe-enrichment scenario (compare the orange and purple lines in the left panel in Fig. 8). Other assumptions, highlighted in the right panel in Fig. 8, affect both $f_{\rm SFR}(Z_{Fe/H}, z)$ and $f_{\rm SFR}(Z_{O/H}, z)$. The assumed (non-)evolution of the FMR at $z > 4$ has a negligible effect on those results compared to $\alpha_{\rm GSMF}$ and $a_{\rm SFR}$.

An alternative approach to comparing $f_{\rm SFR}(Z_{\rm Fe/H}, z)$ and $f_{\rm SFR}(Z_{\rm O/H}, z)$ (which avoids the need for a metallicity threshold) is to examine their MDFs, obtained by integrating the distributions over the selected redshift ranges. This view can help inform the initial metallicity distribution assumptions in models of stellar or prompt-transient populations formed within specific time ranges and serve as a reference for comparison with observed or simulated galactic MDFs. We discuss the MDFs for our models for selected redshift intervals in Appendix E.

[6] Here, we assume the SMC gas phase $Z_{\rm O/H}$ ≈8.2 and $Z_{\rm Fe/H}$=6.85 ([Fe/H]=-0.65 on our solar scale) as in Ch24. However, a broad range of [Fe/H]≈-1 to -0.5 were reported for young SMC stellar samples with ages of a few megayears (e.g. Romaniello et al. 2008; Narloch et al. 2021).

6. <[Fe/H]>: Models and constraints from LGRBs

In Fig. 9, we show the $\langle$[Fe/H]$\rangle_{\rm HI}$ derived from absorption-based LGRB host properties against $\langle$[Fe/H]$\rangle_{\rm SFRD}$ from our model

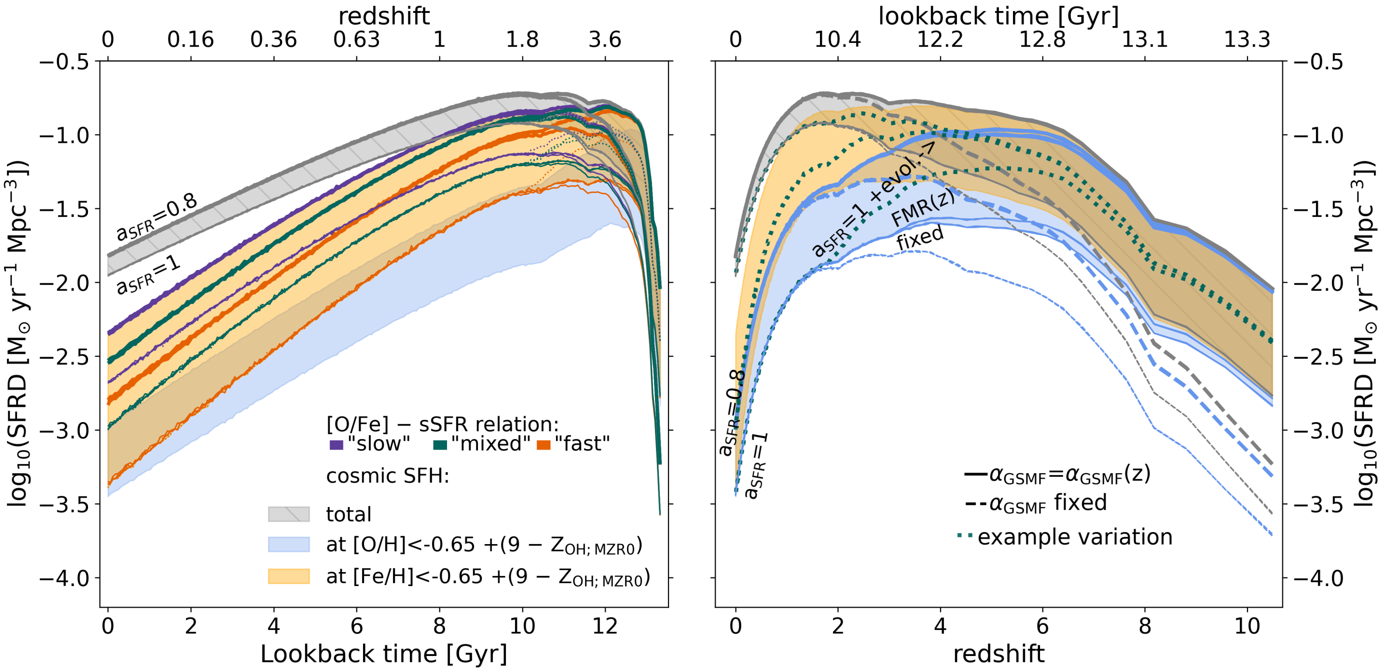

Fig. 8. SFRD as a function of redshift or look-back time. The grey band shows the total SFRD, while the orange (blue) area shows the SFRD at [Fe/H] ([O/H]) below the -0.65 threshold, chosen to roughly select the sub-SMC metallicity environments. The shaded regions indicate the range of results for different model variations with $\alpha_{\rm GSMF}(z)$. Left and right panels: Look-back time and z as the primary x-axes, showing assumptions most relevant at low and high z. The dotted green lines in the right panel show the cSFH and its [Fe/H]<-0.65 and [O/H]<-0.65 cuts for the example variation discussed in Sect. 3. The other lines highlight the selected variations, shown for iron- and oxygen-dependent cSFHs in the left and right panels, respectively. Systematics in $Z_{\rm OH;MZR0}$ translate into shifts in the [O/H] and [Fe/H] thresholds, as shown in the legend.

variations. As discussed in Sect. 3.2.3, the LGRB host sample is not selected by galaxy brightness (i.e. it is not expected to be biased against faint galaxies). Additionally, LGRBs may preferentially occur in low-[Fe/H] and/or high-SFR environments. Consequently, $\langle[\rm Fe/H]\rangle_{\rm HI}$ could be biased to lower values relative to $\langle[\rm Fe/H]\rangle_{\rm SFRD}$, but the offset should decrease with z as LGRB-selected galaxies become increasingly representative of the general star-forming population. In this view, models predicting $\langle[\rm Fe/H]\rangle_{\rm SFRD}$ that fall below the LGRB-based average or diverge from it with increasing z are disfavoured. The current limited sample size and the significant scatter within each z bin (as indicated by the errors in $\langle[\rm Fe/H]\rangle_{\rm HI}$, representing the standard deviation) prevent us from drawing firm conclusions about any of the model variations. Nonetheless, we note the following.

- Assuming $Z_{O/H;MZR0}$ is 0.2 dex lower (long-dashed grey line; within the low z gas-phase $Z_{O/H}$ calibration systematics) variations with 'slow' Fe enrichment (bottom panel) would fall below the LGRB-based average in the lowest z bin – unexpectedly.
- At $z \lesssim 3$, our estimates of $\langle[\rm Fe/H]\rangle_{\rm SFRD}$ are the most sensitive to the adopted [O/Fe]–sSFR relation. The steeper decline between $z = 2$ and 3 obtained under the 'fast' Fe-enrichment assumption (top panel) appears more consistent with the LGRB-based trend when taken at face value.
- The underlying LGRB host population appears insufficiently sampled to enable a reliable estimate of $\langle[\rm Fe/H]\rangle_{\rm HI}$ in the highest-z bin (z = 3–6.4). In this bin, the subsample of LGRB hosts selected to ensure $[\rm M/H]_{\rm tot} \approx$[Fe/H] exhibits less scatter in $[\rm M/H]_{\rm tot}$ compared to both other redshift bins and the full LGRB sample within the same bin. The lower limit on [Fe/H] from GRB 240218A at $z \sim 6.8$ lies $\approx$0.8 dex above the estimated $\langle[\rm Fe/H]\rangle_{\rm HI}$ for z = 3–6.4, further indicating that the small observed scatter is not physical and that the inferred $\langle[\rm Fe/H]\rangle_{\rm HI}$ may be biased.

In light of the above, we avoid drawing conclusions from the highest-z bin. However, differences between our model variations become more pronounced in this regime, and future LGRB constraints could offer a valuable test for our framework. We also show the range of $\langle[\rm O/H]\rangle_{\rm SFRD}$ across our models (pale-blue region in Fig. 9), which is systematically higher than both $\langle[\rm Fe/H]\rangle_{\rm SFRD}$ and $\langle[\rm Fe/H]\rangle_{\rm HI}$.

7. The risks of using solar scaling

The prevalence of super-solar O/Fe abundance ratios contrasts with the fact that the solar abundance pattern is a common underlying assumption in models of stellar evolution, populations, and spectra. This assumption is inherited when such models are used to quantify the effects of stars and stellar populations on their environments and to interpret observations. Enforcing a solar-scaled ratio where it does not apply can introduce systematic errors. The magnitude of these errors is inherently model-dependent; nonetheless, our results can be combined with specific modelling frameworks to quantify the impact in a given application. Here, we restrict ourselves to a qualitative discussion and illustrative examples of the expected biases.

7.1. Pedagogical example

In models and simulations, metallicity effects are often parametrised by simple scaling with the total metal-mass fraction relative to solar ($Z/Z_\odot$). In practice, however, particular elements may dominate 'metallicity' effects for different physical processes. In particular, gas cooling is largely determined by

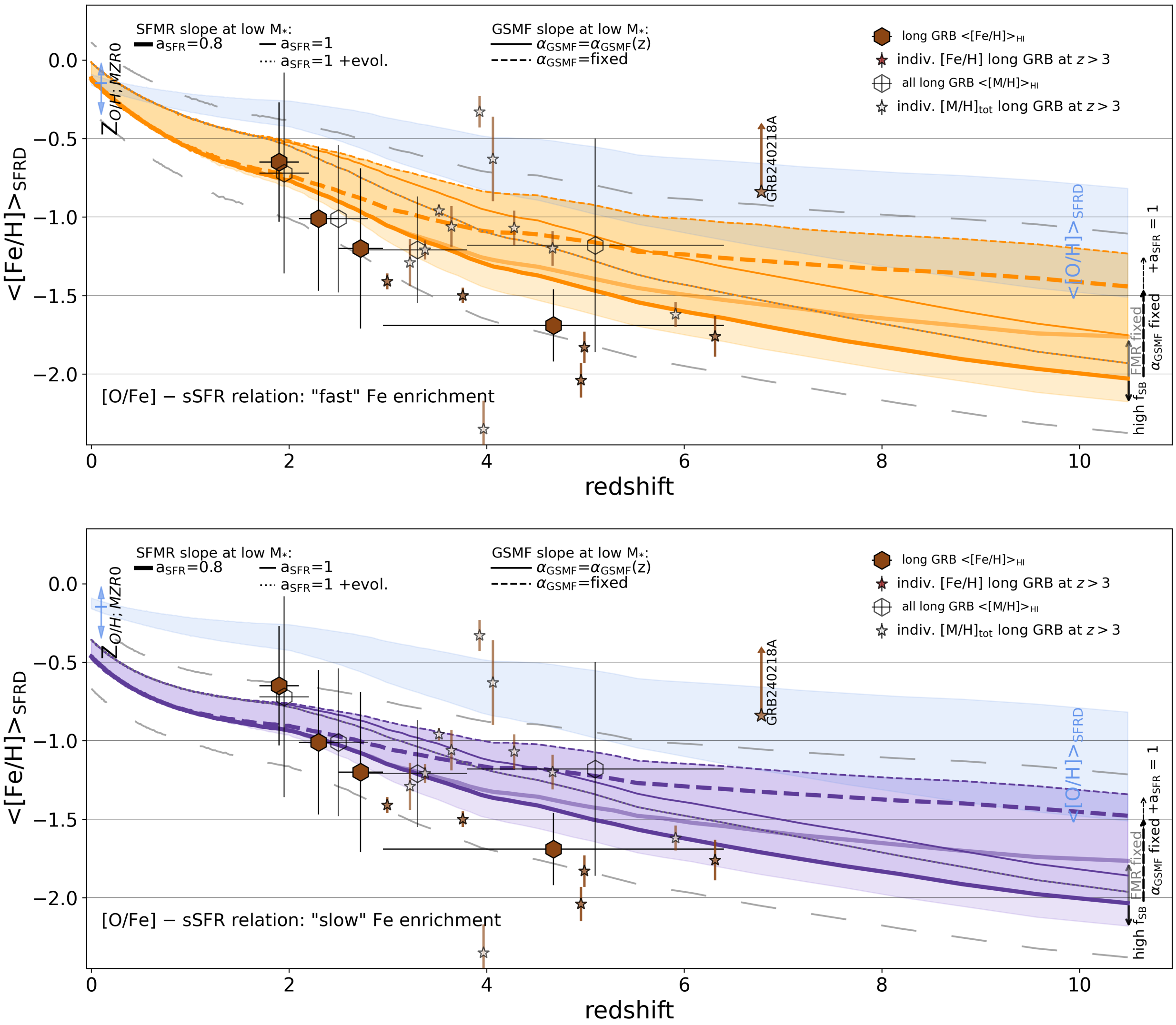

Fig. 9. SFRD-weighted mean $\langle[\mathrm{Fe/H}]\rangle_{\mathrm{SFRD}}$ as a function of redshift for all our models (orange and purple regions) with selected variations shown as lines. The corresponding $\langle[\mathrm{O/H}]\rangle_{\mathrm{SFRD}}$ range is shown in pale blue (same in both panels). Top and bottom panels: [O/Fe]–sSFR relation with 'fast' and 'slow' Fe enrichment. The data points indicate the $\langle[\mathrm{Fe/H}]\rangle_{\mathrm{HI}}$ values from the absorption-derived LGRB hosts (filled hexagons: subsample with more accurate dust corrections, open hexagons: full sample; vertical and horizontal errors represent standard deviation and z-bin width, respectively). The stars indicate individual $z > 3$ LGRB hosts (brown: with more accurate dust corrections for which $[\mathrm{M/H}]_{\mathrm{tot}} \approx[\mathrm{Fe/H}]$; white: remaining objects, for which $[\mathrm{M/H}]_{\mathrm{tot}}$ may overestimate [Fe/H]). The vertical arrows represent the systematics in our estimates resulting from $Z_{O/H}$ calibration (affecting both $\langle[\mathrm{Fe/H}]\rangle_{\mathrm{SFRD}}$ and $\langle[\mathrm{O/H}]\rangle_{\mathrm{SFRD}}$). The dashed grey lines show its effect at the edges of the $\langle[\mathrm{Fe/H}]\rangle_{\mathrm{SFRD}}$ range.

the abundance of oxygen (Richings et al. 2014; Katz et al. 2022; Sharda et al. 2023), while the effects of stellar evolution (e.g. feedback and winds) are driven by the abundance of iron (see Sect. 7.2). If [O/Fe]=0, one may apply the same scaling to describe both processes, i.e. $\mathrm{n_{O/H}/n_{O/H_\odot}} = \mathrm{n_{Fe/H}/n_{Fe/H_\odot}} = \mathrm{Z/Z_\odot}$. However, our results show that this is rarely the case. As a simple illustration of the bias introduced by this scaling, one can compare the difference in $n_{O/H}$ and $n_{Fe/H}$ when $Z/Z_\odot$ is fixed but computed for an arbitrary [O/Fe] (all the other elements are solar-scaled). Assuming $[\mathrm{O/Fe}]=[\mathrm{O/Fe}]_{\mathrm{CCSN}}=0.52$ as well as mass fractions of $X_O/Z_\odot \approx 0.5$ and $X_{Fe}/Z_\odot \approx 0.09$ in the solar composition (Grevesse & Sauval 1998),

$$\left(\frac{\mathrm{n_{O/H}}}{\mathrm{n_{O/H_\odot}}}\right) / \left(\frac{Z}{Z_\odot}\right) = \frac{(X_O+X_{Fe})\ 10^{[\mathrm{O/Fe}]}}{X_{Fe}+X_O\ 10^{[\mathrm{O/Fe}]}} \approx 1.12,$$

$$\left(\frac{\mathrm{n_{Fe/H}}}{\mathrm{n_{Fe/H_\odot}}}\right) / \left(\frac{Z}{Z_\odot}\right) = \frac{(X_O+X_{Fe})}{X_{Fe}+X_O\ 10^{[\mathrm{O/Fe}]}} \approx 0.35.$$

Thus, using $Z/Z_\odot$ scaling would overpredict $n_{O/H}$-scaled effects by only a small amount (12%) but underpredict $n_{Fe/H}$-scaled effects by a factor of 3 in young and highly star-forming environments, biasing modelled cooling and feedback in opposite directions. In general, the difference is greater for elements that contribute less by mass.

7.2. Evolution of stars and stellar multiples

Stellar evolution is sensitive to birth chemical composition predominantly via effect on winds, opacity, and nuclear burning efficiency. For stars with $M_{\mathrm{ZAMS}} \gtrsim 1.2, M_\odot$ whose main-sequence burning is CNO-cycle dominated, the nuclear rate depends directly on the total CNO abundance (Kippenhahn et al. 2012). The main impact is on the main-sequence lifetime, shortened by a few percent if $Z_{\mathrm{O/H}}$ increases at fixed $Z_{\mathrm{Fe/H}}$ (Pietrinferni et al. 2009; VandenBerg et al. 2012). The effects of opacity and line-driven winds are more striking and increasingly significant for hot, massive stars. Photospheric and envelope opacities are set largely by Fe-group abundances (Iglesias & Rogers 1996;

oxygen dominates only in the cool atmospheres of late-K or M dwarfs and giants) and the radiation-driven winds of hot stars scale with $Z_{\rm Fe/H}$ (e.g. Pauldrach et al. 1993; Kudritzki 2002; Vink & de Koter 2005; Puls et al. 2008; Krtička & Kubát 2018; Vink & Sander 2021; Björklund et al. 2023). Mass loss is weaker at lower $Z_{\rm Fe/H}$, though the scaling also depends on stellar effective temperatures, mass, and luminosity. Adopting $\dot{M}_{\rm wind} \propto Z_{Fe/H}^{\alpha_{wind}}$ with α_{wind} = 0.42 or α_{wind} =0.85 (Vink & Sander 2021, above and below their bi-stability jump, respectively) in young and strongly star-forming environments where [O/Fe] ≈ [O/Fe]$_{\rm CCSN}$, one may overestimate $\dot{M}_{\rm wind}$ by a factor of ∼ 1.7 – 2.7 using $Z_{\rm O/H}$ as a solar-scaled proxy for $Z_{\rm Fe/H}$. A more striking yet uncertain example is that of very massive stars (VMSs; $\gtrsim$ 100 $M_\odot$), which can drive optically thick winds with $\dot{M}_{\rm wind}$ that exceed that of canonical OB stars (Gräfener & Hamann 2008; Vink et al. 2011; Goswami et al. 2022; Sabhahit et al. 2023; Costa et al. 2025; Martins et al. 2025). Such winds cause a VMS to lose most of its mass over the main sequence. However, constraints are currently lacking at sub-Large Magellanic Cloud (LMC) metallicities. Sabhahit et al. (2023) proposed a $Z_{\rm Fe/H}$-dependent condition for launching strong optically thick winds, which requires the VMS to be more extreme (i.e. more massive and luminous) at lower $Z_{\rm Fe/H}$. In the presence of such a threshold, incorrectly assigning a metallicity (and thus the wind mode) could affect the masses of the star and the remnant black hole (BH) by an order of magnitude. Using $Z_{\rm O/H}$ as a solar-scaled proxy for $Z_{\rm Fe/H}$ would lead to an overestimation of the strong wind phenomenon in VMS and underestimation of remnant masses, particularly at low $Z_{\rm Fe/H}$. In summary, $Z_{\rm Fe/H}$-dependent wind mass loss appears to be the main driver of metallicity effects on the evolution of massive stars (including in binaries and multiples). In binaries, composition-dependent radius evolution is another key factor, as it shifts when (and if) Roche-lobe overflow occurs, altering the mode, stability, and outcome of mass transfer (e.g. Sect. 2 in Costa et al. 2024, and references therein). The radii of massive stars are uncertain, but their sensitivity to metallicity is mostly due to changes in opacity and, to a lesser extent, nuclear burning efficiency (Xin et al. 2022). In the absence of self-consistent massive star and binary models with non-solar abundance patterns representative of the considered environments, $Z_{\rm Fe/H}$ provides a practical scaling of their metallicity dependence. Conversely, relying on $Z_{\rm O/H}$ (or α-elements) yields the largest errors.

7.3. Galaxy and stellar population spectra and diagnostics

Models with non-solar and solar -scaled abundances differ in their predictions for both stellar evolution (isochrones and evolutionary tracks) and atmospheres. In models of old populations (which formed when <[O/Fe]>$_{\rm SFRD}$ was high; e.g. ellipticals and GCs), the key differences lie in colours, particularly for turnoff and subgiant branch stars used as age indicators, resulting in biased age determinations if ignored (e.g. Trager et al. 2000; Thomas & Maraston 2003; Vazdekis et al. 2015; Coelho 2014; Pietrinferni et al. 2021; Knowles et al. 2023; Park et al. 2025). Large grids of α-enhanced evolutionary models of (very) massive stars, which provide the basis for self-consistent SPS models suitable for interpreting young, highly star-forming environments typical of high-z galaxies, have only recently begun to appear in the literature (Grasha et al. 2021; Byrne et al. 2022, 2025). In massive-star dominated populations, the key differences lie in the UV continuum, ionising outputs, and UV wind features. These are primarily driven by $Z_{\rm Fe/H}$ rather than non-solar [O/Fe] per se (see Sect. 7.2). In general, a young stellar population at lower $Z_{\rm Fe/H}$ is more UV-bright and produces a harder ionising spectrum (e.g. Leitherer et al. 1999; Smith et al. 2002; Stanway et al. 2016; Stanway & Eldridge 2018). Using $Z_{\rm O/H}$ as a proxy for $Z_{\rm Fe/H}$ when deriving SFR with common UV diagnostics (e.g. Bicker & Fritze-v. Alvensleben 2005; Hao et al. 2011; Kennicutt & Evans 2012; Madau & Dickinson 2014) would lead to an overestimation in environments with [O/Fe]>0. Furthermore, ignoring the fact that in such environments iron-poor stars ionise relatively oxygen-rich nebulae can lead to a misinterpretation of stellar and nebular diagnostics (e.g. Steidel et al. 2016; Trainor et al. 2016; Strom et al. 2017). As gas cooling and heating are determined by $Z_{\rm O/H}$ and $Z_{\rm Fe/H}$, respectively, this can be effectively accounted for in the models by adopting different metallicities for the stellar and gas components (Strom et al. 2018; Sanders et al. 2021; Runco et al. 2021; Strom et al. 2022).

7.4. Transients and phenomena linked to metal-poor progenitors

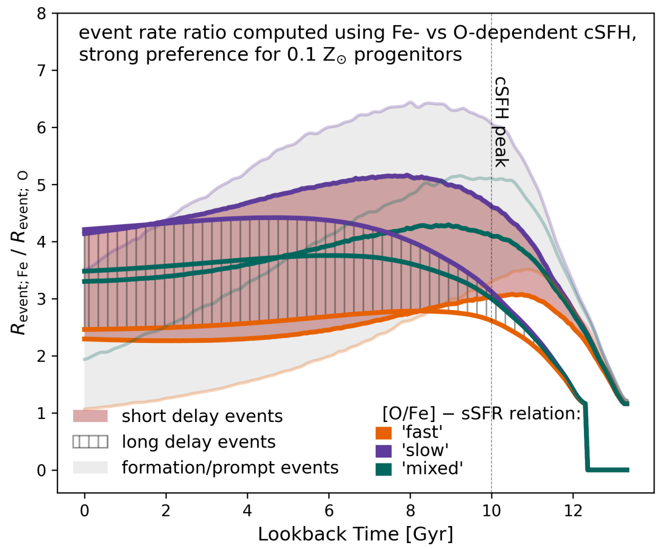

Fig. 10. Relative rate density of events originating from metal-poor progenitors, obtained using $f_{\rm SFR}(Z_{\rm Fe/H}, t)$ and $f_{\rm SFR}(Z_{\rm O/H}, t)$ as a function of look-back time. The grey area indicates the prompt events, or, equivalently, the formation rate of delayed events. The brown and hatched areas indicate events with a distribution of delays, peaked at short (10 Myr) and long (1 Gyr) delay times with respect to star formation, respectively. The coloured lines distinguish the assumptions on the [O/Fe]-sSFR relation. The alternative assumptions relevant for $f_{\rm SFR}(Z_{\rm Fe/H}, t)$ and $f_{\rm SFR}(Z_{\rm O/H}, t)$ are the same as for the example variation from Sect. 3. The vertical line indicates the peak time of the cSFH. Using $f_{\rm SFR}(Z_{O/H}, t)$ underestimates the metal-poor event rates by a redshift- (and model-) dependent factor.

The uncertainty and difference between the $Z_{\rm Fe/H}$ and $Z_{\rm O/H}$ -dependent cSFH is the largest in the metal-poor regime. This is also where many transients of stellar-origin appear more common and/or more luminous. These include X-ray sources (Kovlakas et al. 2020; Fornasini et al. 2020; Lehmer et al. 2021), LGRBs ,and hydrogen-poor superluminous supernovae (Lunnan et al. 2014; Schulze et al. 2018) or luminous fast blue optical transients (Coppejans et al. 2020; Chrimes et al. 2024b,a; Klencki & Metzger 2025). Phenomena theorised to prefer metal-poor progenitors also include stellar BH mergers (Belczynski et al. 2010b; Belczynski et al. 2016; Klencki et al. 2018; Giacobbo et al. 2018; Chruslinska et al. 2019; Neijssel et al. 2019; Broekgaarden et al. 2022; Iorio et al. 2023; Chruślińska 2024), pair-instability supernovae (Woosley et al. 2002; Stevenson et al. 2019; Sabhahit et al. 2023), and chemically homogeneous evolution (Yoon & Langer 2005; Yoon et al. 2006; Szécsi et al. 2015; Marchant et al. 2016; Mandel & de Mink 2016). Stellar BHs with masses $\gtrsim 30 M_{\odot}$, found in a substantial fraction ($\gtrsim$40%) BH merger events detected with GW (LIGO Scientific Collaboration et al. 2025), may also require subsolar progenitors (Belczynski et al. 2010a; Romagnolo et al. 2024; Vink et al. 2024; Merritt et al. 2025). Furthermore, ionising spectra harder than those predicted by existing SPS models are required to explain the emission properties of metal-poor galaxies (Senchyna et al. 2017; Schaerer et al. 2019; Katz et al. 2023; Telford et al. 2023). Overall, it appears that stellar evolution is more likely to produce (more of the) extreme phenomena at lower metallicities. However, the driving factors and the regime in which these can occur remain unclear. As in the above examples, most of the empirical constraints come from stellar and transient populations. These require metallicity-dependent cSFH as part of the modelling and interpretation.

In Fig. 10 we present a simple estimate of the relative occurrence rate of events with a strong preference for low-metallicity progenitors calculated using $f_{\rm SFR}(Z_{\rm Fe/H},t)$ and $f_{\rm SFR}(Z_{\rm O/H},t)$. Assuming that in the context of stellar-origin transients and phenomena 'metallicity'$\approx Z_{\rm Fe/H}$, this serves to show the bias introduced by the use of metallicity-dependent cSFH based on an incorrect probe. We note that the result shown in Fig. 10 is model-dependent and it should be taken as a 'sign and order-of-magnitude' calculation. The event rate $R_{\rm event;X}$ follows from

$$R_{\rm event;X}(t_0) = \int_0^{t_0} \int f_{\rm SFR}(Z_{X/H},\, t')\; \eta(Z_{X/H})\; p_{\rm delay}(t_0 - t')\;\, dZ_{X/H}\, dt', \quad (2)$$

where the index 'X' denotes either oxygen (X=O) or iron (X=Fe). Here, $\eta(Z_{X/H})$ stands for the event progenitor formation efficiency (number per unit stellar mass formed) as a function of metallicity, for which we used a logistic function (used in the context of LGRBs, hydrogen-poor superluminous SNe, BH mergers, c.f. Schulze et al. 2018; Chruślińska 2024; Disberg et al. 2025):

$$\eta(Z_{X/H}) = \eta_{high} + (\eta_{low} - \eta_{high})/(1. + \exp(-k \cdot (Z_{X/H} - Z_{X/H_{thr}}))), \quad (3)$$

with $k = -10$, which yields a sharp decrease from η_{low} to η_{high} with a midpoint at $Z_{X/H_{thr}}$. We set this midpoint value to 1/10 of the solar oxygen/iron abundance. We furthermore assumed $\eta_{high} = \eta_{low}/100$, i.e. the formation efficiency is not fully truncated at high $Z_{X/H}$ but drops by two orders of magnitude with respect to the plateau η_{low} at low $Z_{X/H}$. Since we only compare the relative rate, the η_{low} value is irrelevant. For the delay time distribution, we assumed the power law

$$p_{\rm delay}(\tau) = \begin{cases} \propto \tau^{-1}, & \tau \geq \tau_{\rm event;min}, \\ 0, & \tau < \tau_{\rm event;min}, \end{cases} \quad (4)$$

normalised to unity between $\tau_{\rm event;min}$ and Hubble time. This is a conventional approximation for $p_{\rm delay}$ of gravitational wave sources (e.g. BH mergers). We use $\tau_{\rm event;min}$=10 Myr and 1 Gyr for events with a 'short' (brown region) and 'long' delay (hatched region), respectively, for the examples shown in Fig. 10. Both short and long delays are possible for BH mergers within the formation scenarios considered in the literature. Replacing the $p_{\rm delay}$ with a Dirac delta at zero, Eq. 2 can be used to compute the formation rate and prompt event rate (e.g. LGRB and supernovae). We note the following.

- Using $f_{\rm SFR}(Z_{O/H},t)$ underestimates metal-poor event rates. The difference varies with cosmic time.
- The difference depends on $f_{\rm SFR}(Z_{Fe/H},t)$ model variation and is the largest for variations with the largest difference between O- and Fe- dependent cSFH (in particular for the 'slow' Fe enrichment model family).
- The difference also depends on $p_{\rm delay}$ (larger for prompt events) and $\eta(Z_{X/H})$ (larger for more extreme metallicity threshold or metallicity dependence).
- $f_{\rm SFR}(Z_{Fe/H},t)$ model variation affects the metal-poor event rate evolution over cosmic time. In particular, the uncertainty in the [O/Fe]-sSFR relation alone affects the evolution, peak location, and the magnitude of the rate (by factor of 2-3).

Variations in $R_{\rm event}$ due to the uncertainty in $f_{\rm SFR}(Z_{Fe/H},t)$ across our variations are typically within a factor of a few but can reach $\sim O(10)$ for more extreme $\eta(Z_{Fe/H})$ and $p_{\rm delay}$ assumptions than those chosen for our example. The bias introduced by the $f_{\rm SFR}(Z_{O/H},t)$ and the uncertainty in $f_{\rm SFR}(Z_{Fe/H},t)$ are both important when considering transients and phenomena sensitive to low metallicity.

8. Conclusions

Oxygen and iron are key to different astrophysical processes and are primarily produced by nucleosynthetic sources operating on different timescales. Their relative abundances in the interstellar medium varies over time and can significantly depart from the solar ratio. However, observationally, it is often only possible to constrain one of these two elemental abundances, which is then used as a representative proxy for metallicity after being scaled to the solar abundance. Usually, the different roles and evolution of these elements are not distinguished in models and simulations that use a total metal mass fraction to parametrise the effects of metallicity on different processes. In this work, we proposed a framework to overcome these observational limitations and provide more appropriate scaling for the cosmic evolution of the abundances of oxygen and iron used in models.

Building on Paper I Ch24, which introduced and empirically constrained the theoretical underpinnings of the redshift-invariant [O/Fe]–sSFR relation of galaxies, we applied this relation to derive the iron-dependent cSFH, $f_{\rm SFR}(Z_{\rm Fe/H},t)$, alongside its oxygen-based counterpart, $f_{\rm SFR}(Z_{\rm O/H},t)$. Here, we extended and validated the observation-based framework of ChN19; Ch21 against more recent and additional empirical constraints. We also introduced several model variations to bracket the main uncertainties in the core ingredients of our framework, i.e. the distributions of galaxy SFR , $Z_{O/H}$, GSMF, and the [O/Fe]–sSFR relation. This allowed us to quantify how these uncertainties propagate to the final result. Notably, the high-z JWST results constrain the evolution of the FMR and MZR at $z > 3$ enough so that it is no longer the dominant source of uncertainty in our $f_{\rm SFR}(Z_{\rm O/H},t)$ estimates. Our main conclusions are the following:

- Star formation with a near-solar [O/Fe] abundance is rare throughout cosmic history. The bulk (at least 70% across our variations) of the integrated stellar mass formed with O/Fe greater than the solar abundance ratio.

– The SFRD-weighted average metallicity is lower when using [Fe/H] than [O/H] at all redshifts, except when the [O/Fe]–sSFR relation resembles our 'fast Fe-enrichment' case, for which $\langle[\mathrm{O/Fe}]\rangle_{\mathrm{SFRD}}$ may become subsolar at $z \lesssim 0.4$ (Fig. 5).
– The offset between $\langle[\mathrm{Fe/H}]\rangle_{\mathrm{SFRD}}$ and $\langle[\mathrm{O/H}]\rangle_{\mathrm{SFRD}}$ increases to $z \approx 3$ and approaches a roughly constant value at higher redshifts ([O/Fe]≈0.4-0.5 dex, i.e. up to the CCSN-ratio; Fig. 5). This offset depends primarily on the [O/Fe]–sSFR relation (particularly on the assumed $[\mathrm{O/Fe}]_{\mathrm{CCSN}}$ for CCSNe and the minimum delay for enhanced Fe enrichment) and on the galaxy SFR distribution.
– The differences between $f_{\mathrm{SFR}}(Z_{\mathrm{O/H}}, t)$ and $f_{\mathrm{SFR}}(Z_{\mathrm{Fe/H}}, t)$ are the largest in the low-metallicity and high-z regimes. These differences are the smallest if the delay in the enhanced Fe enrichment relative to star formation is minimal (our 'fast Fe-enrichment' case; see Figs. 4 and 8).
– The absorption-derived $\langle[\mathrm{Fe/H}]\rangle_{\mathrm{HI}}(z)$ from LGRB afterglow–selected sources is broadly consistent with our $\langle[\mathrm{Fe/H}]\rangle_{\mathrm{SFRD}}(z)$ estimates and is offset from $\langle[\mathrm{O/H}]\rangle_{\mathrm{SFRD}}(z)$ (Fig. 9). While the current comparison is not constraining for our models, a larger sample (particularly at $z > 4$) could provide the most direct tests of our $f_{\mathrm{SFR}}(Z_{\mathrm{Fe/H}}, t)$ framework.

These results underscore that 'metallicity' estimates based on oxygen (or α-elements in general) and iron-group probes are not interchangeable. Failing to account for non-solar abundance ratios may lead to important biases and systematic errors. In particular, in environments with [O/Fe] > 0,

– relying on solar abundance scaling would slightly overpredict O-scaled effects (e.g. gas cooling) and underpredict Fe-scaled effects (e.g. stellar feedback, by up to a factor of ∼ 3);
– using $Z_{\mathrm{O/H}}$ as a solar-scaled proxy for $Z_{\mathrm{Fe/H}}$ overestimates hot-star and VMS wind mass-loss effects. This non-trivially affects the evolution of stars and stellar multiples, UV and ionising stellar spectra (SFR and metallicity diagnostics), properties of stellar BHs, and transients of massive-star origin;
– using $f_{\mathrm{SFR}}(Z_{O/H}, t)$ instead of $f_{\mathrm{SFR}}(Z_{Fe/H}, t)$ underestimates the rates of events and phenomena linked to metal-poor progenitors (e.g. LGRBs and stellar BH mergers) by a z-dependent factor, complicating the interpretation of z-trends in their population properties (Fig. 10).

The magnitude of these effects is model-dependent. Our results can be used within specific frameworks to alleviate and quantify these biases. Finally, we emphasise that we obtain the above results simultaneously predicting that galaxies with MW-like M_* are among the dominant contributors to the cosmic SFRD at $z \lesssim 2$ and can form stars with the Sun's $Z_{\mathrm{O/H}}$ and $Z_{\mathrm{Fe/H}}$ at the solar birth epoch. However, for model variations with long ($\gtrsim 10^8$yr) delays in enhanced Fe enrichment (our 'slow Fe-enrichment' case) such stars would not coincide with the MDF peak in MW-like galaxies.

9. Data availability

Data generated during this study and code underlying our analysis are available via Zenodo `https://doi.org/10.5281/zenodo.18018782` and GitHub `https://github.com/Mchruslinska/MetalCosfr_public.git`.

Acknowledgements. MCh would like to thank T. Matsuno and J. Klencki for their insightful comments, and K. Heintz for the discussion on the LGRB sample. We thank the anonymous referee for the comments and suggestions that have helped us to improve the paper.
Software: matplotlib (Hunter 2007), scipy (Virtanen et al. 2020), numpy (Harris et al. 2020), astropy (Astropy Collaboration et al. 2013; Collaboration et al. 2018).

References

Adamo, A., Hollyhead, K., Messa, M., et al. 2020a, MNRAS, 499, 3267
Adamo, A., Zeidler, P., Kruijssen, J. M. D., et al. 2020b, Space Sci. Rev., 216, 69
Algera, H. S. B., Inami, H., Oesch, P. A., et al. 2023, MNRAS, 518, 6142
Amarsi, A. M., Nissen, P. E., & Skúladóttir, Á. 2019, A&A, 630, A104
Andrews, B. H. & Martini, P. 2013, ApJ, 765, 140
Arellano-Córdova, K. Z., Esteban, C., García-Rojas, J., & Méndez-Delgado, J. E. 2020, MNRAS, 496, 1051
Asplund, M., Amarsi, A. M., & Grevesse, N. 2021, A&A, 653, A141
Asplund, M., Grevesse, N., Sauval, A. J., & Scott, P. 2009, ARA&A, 47, 481
Astropy Collaboration, Robitaille, T. P., Tollerud, E. J., et al. 2013, A&A, 558, A33
Baldry, I. K., Driver, S. P., Loveday, J., et al. 2012, MNRAS, 421, 621
Belczynski, K., Bulik, T., Fryer, C. L., et al. 2010a, ApJ, 714, 1217
Belczynski, K., Dominik, M., Bulik, T., et al. 2010b, ApJ, 715, L138
Belczynski, K., Holz, D. E., Bulik, T., & O'Shaughnessy, R. 2016, Nature, 534, 512
Bellazzini, M., Muraveva, T., & Garofalo, A. 2025, A&A, 698, L10
Belokurov, V. & Kravtsov, A. 2024, MNRAS, 528, 3198
Berger, E., Penprase, B. E., Cenko, S. B., et al. 2006, ApJ, 642, 979
Bezanson, R., Labbe, I., Whitaker, K. E., et al. 2024, ApJ, 974, 92
Bian, F., Kewley, L. J., & Dopita, M. A. 2018, ApJ, 859, 175
Bicker, J. & Fritze-v. Alvensleben, U. 2005, A&A, 443, L19
Bisigello, L., Caputi, K. I., Grogin, N., & Koekemoer, A. 2018, A&A, 609, A82
Björklund, R., Sundqvist, J. O., Singh, S. M., Puls, J., & Najarro, F. 2023, A&A, 676, A109
Boco, L., Lapi, A., Chruslinska, M., et al. 2021, ApJ, 907, 110
Boogaard, L. A., Brinchmann, J., Bouché, N., et al. 2018, A&A, 619, A27
Bresolin, F., Kudritzki, R.-P., & Urbaneja, M. A. 2022, ApJ, 940, 32
Bresolin, F., Kudritzki, R.-P., Urbaneja, M. A., et al. 2016, ApJ, 830, 64
Briel, M. M., Fragos, T., Salafia, O. S., et al. 2025, A&A, 701, A84
Brinchmann, J., Charlot, S., White, S. D. M., et al. 2004, MNRAS, 351, 1151
Broekgaarden, F. S., Berger, E., Stevenson, S., et al. 2022, MNRAS, 516, 5737
Bromm, V. & Loeb, A. 2003, Nature, 425, 812
Buder, S., Sharma, S., Kos, J., et al. 2021, MNRAS, 506, 150
Bunker, A. J., Saxena, A., Cameron, A. J., et al. 2023, A&A, 677, A88
Byrne, C. M., Eldridge, J. J., & Stanway, E. R. 2025, MNRAS, 537, 2433
Byrne, C. M., Stanway, E. R., Eldridge, J. J., McSwiney, L., & Townsend, O. T. 2022, MNRAS, 512, 5329
Caputi, K. I., Deshmukh, S., Ashby, M. L. N., et al. 2017, ApJ, 849, 45
Carretta, E., Bragaglia, A., Gratton, R., & Lucatello, S. 2009, A&A, 505, 139
Casagrande, L., Schönrich, R., Asplund, M., et al. 2011, A&A, 530, A138
Casey, C. M., Zavala, J. A., Spilker, J., et al. 2018, ApJ, 862, 77
Catelan, M. 2004, in Astronomical Society of the Pacific Conference Series, Vol. 310, IAU Colloq. 193: Variable Stars in the Local Group, ed. D. W. Kurtz & K. R. Pollard, 113
Catelan, M. 2009, Ap&SS, 320, 261
Chemerynska, I., Atek, H., Dayal, P., et al. 2024, ApJ, 976, L15
Chrimes, A. A., Coppejans, D. L., Jonker, P. G., et al. 2024a, A&A, 691, A329
Chrimes, A. A., Jonker, P. G., Levan, A. J., et al. 2024b, MNRAS, 527, L47
Chrimes, A. A., Stanway, E. R., & Eldridge, J. J. 2020, MNRAS, 491, 3479
Christensen, L., Hjorth, J., & Gorosabel, J. 2004, A&A, 425, 913
Chruślińska, M. 2024, Annalen der Physik, 536, 2200170
Chruślińska, M. & Nelemans, G. 2019, MNRAS, 488, 5300
Chruslinska, M., Nelemans, G., & Belczynski, K. 2019, MNRAS, 482, 5012
Chruślińska, M., Nelemans, G., Boco, L., & Lapi, A. 2021, MNRAS, 508, 4994
Chruślińska, M., Pakmor, R., Matthee, J., & Matsuno, T. 2024, A&A, 686, A186
Clementini, G., Ripepi, V., Garofalo, A., et al. 2023, A&A, 674, A18
Coelho, P. R. T. 2014, MNRAS, 440, 1027
Collaboration, T. A., Price-Whelan, A. M., Sipőcz, B. M., et al. 2018, AJ, 156, 123
Coppejans, D. L., Margutti, R., Terreran, G., et al. 2020, ApJ, 895, L23
Costa, G., Chrušlińska, M., Klencki, J., et al. 2024, in Black Holes in the Era of Gravitational-Wave Astronomy, ed. M. Arca Sedda, E. Bortolas, & M. Spera, 1–148
Costa, G., Shepherd, K. G., Bressan, A., et al. 2025, A&A, 694, A193
Crain, R. A., Schaye, J., Bower, R. G., et al. 2015, MNRAS, 450, 1937
Cresci, G., Mannucci, F., & Curti, M. 2019, A&A, 627, A42
Cullen, F., Shapley, A. E., McLure, R. J., et al. 2021, MNRAS, 505, 903
Curti, M., Cresci, G., Mannucci, F., et al. 2017, MNRAS, 465, 1384
Curti, M., D'Eugenio, F., Carniani, S., et al. 2023, MNRAS, 518, 425

Curti, M., Maiolino, R., Curtis-Lake, E., et al. 2024, A&A, 684, A75
Curti, M., Mannucci, F., Cresci, G., & Maiolino, R. 2020, MNRAS, 491, 944
Davé, R., Finlator, K., & Oppenheimer, B. D. 2011, MNRAS, 416, 1354
De Cia, A., Ledoux, C., Mattsson, L., et al. 2016, A&A, 596, A97
De Cia, A., Ledoux, C., Petitjean, P., & Savaglio, S. 2018, A&A, 611, A76
De Cia, A., Roman-Duval, J., Konstantopoulou, C., et al. 2024, A&A, 683, A216
De Rossi, M. E., Bower, R. G., Font, A. S., Schaye, J., & Theuns, T. 2017, MNRAS, 472, 3354
Di Cesare, C., Matthee, J., Naidu, R. P., et al. 2026, A&A, 707, A129
Disberg, P., Lankreijer, A., Chruślińska, M., et al. 2025, A&A, 703, A288
Donnan, C. T., McLure, R. J., Dunlop, J. S., et al. 2024, MNRAS, 533, 3222
Eldridge, J. J. & Stanway, E. R. 2022, ARA&A, 60, 455
Ellison, S. L., Patton, D. R., Simard, L., & McConnachie, A. W. 2008, ApJ, 672, L107
Feuillet, D. K., Frankel, N., Lind, K., et al. 2019, MNRAS, 489, 1742
Finkelstein, S. L., Bagley, M. B., Ferguson, H. C., et al. 2023, ApJ, 946, L13
Fornasini, F. M., Civano, F., & Suh, H. 2020, MNRAS, 495, 771
Fruchter, A. S., Levan, A. J., Strolger, L., et al. 2006, Nature, 441, 463
Galama, T. J., Vreeswijk, P. M., Van Paradijs, J., et al. 1998, Nature, 395, 670
Gallazzi, A., Charlot, S., Brinchmann, J., White, S. D. M., & Tremonti, C. A. 2005, MNRAS, 362, 41
Garcia, A. M., Torrey, P., Ellison, S. L., et al. 2024, arXiv e-prints, arXiv:2407.06254
Garcia, M., Evans, C. J., Bestenlehner, J. M., et al. 2021, Experimental Astronomy, 51, 887
Giacobbo, N., Mapelli, M., & Spera, M. 2018, MNRAS, 474, 2959
Goswami, S., Silva, L., Bressan, A., et al. 2022, A&A, 663, A1
Götberg, Y., de Mink, S. E., Groh, J. H., Leitherer, C., & Norman, C. 2019, A&A, 629, A134
Götberg, Y., de Mink, S. E., McQuinn, M., et al. 2020, A&A, 634, A134
Gräfener, G. & Hamann, W. R. 2008, A&A, 482, 945
Graham, J. F., Schady, P., & Fruchter, A. S. 2023, ApJ, 954, 13
Grand, R. J. J., Gómez, F. A., Marinacci, F., et al. 2017, MNRAS, 467, 179
Grasha, K., Roy, A., Sutherland, R. S., & Kewley, L. J. 2021, ApJ, 908, 241
Greggio, L. 2005, A&A, 441, 1055
Greggio, L. 2010, MNRAS, 406, 22
Grevesse, N. & Sauval, A. J. 1998, Space Sci. Rev., 85, 161
Grimmett, J. J., Müller, B., Heger, A., Banerjee, P., & Obergaulinger, M. 2021, MNRAS, 501, 2764
Grudić, M. Y., Kruijssen, J. M. D., Faucher-Giguère, C.-A., et al. 2021, MNRAS, 506, 3239
Gruppioni, C., Béthermin, M., Loiacono, F., et al. 2020, A&A, 643, A8
Hamadouche, M. L., McLure, R. J., Carnall, A., et al. 2024, arXiv e-prints, arXiv:2412.09592
Hao, C.-N., Kennicutt, R. C., J., Johnson, B. D., Calzetti, D., et al. 2011, ApJ, 741, 124
Harris, C. R., Millman, K. J., van der Walt, S. J., et al. 2020, Nature, 585, 357
Hayden, M. R., Bovy, J., Holtzman, J. A., et al. 2015, ApJ, 808, 132
Heger, A., Fryer, C. L., Woosley, S. E., Langer, N., & Hartmann, D. H. 2003, ApJ, 591, 288
Heger, A., Müller, B., & Mandel, I. 2023, in The Encyclopedia of Cosmology. Set 2: Frontiers in Cosmology. Volume 3: Black Holes, ed. Z. Haiman, 61–111
Heger, A. & Woosley, S. E. 2002, ApJ, 567, 532
Heintz, K. E., Brammer, G. B., Giménez-Arteaga, C., et al. 2023, Nature Astronomy, 7, 1517
Henry, A., Rafelski, M., Sunnquist, B., et al. 2021, ApJ, 919, 143
Hernandez, S., Aloisi, A., James, B. L., et al. 2021, ApJ, 908, 226
Hinshaw, G., Larson, D., Komatsu, E., et al. 2013, ApJS, 208, 19
Hirschi, R., Meynet, G., & Maeder, A. 2005, A&A, 443, 581
Hjorth, J., Sollerman, J., Møller, P., et al. 2003, Nature, 423, 847
Hunter, J. D. 2007, Computing Sci. Eng., 9, 90
Iben, I., J. & Tutukov, A. V. 1984, ApJS, 54, 335
Iglesias, C. A. & Rogers, F. J. 1996, ApJ, 464, 943
Inkenhaag, A., Schady, P., Wiseman, P., et al. 2025, MNRAS[arXiv:2506.08114]
Iorio, G., Mapelli, M., Costa, G., et al. 2023, MNRAS, 524, 426
Janka, H. T., Langanke, K., Marek, A., Martínez-Pinedo, G., & Müller, B. 2007, Phys. Rep., 442, 38
Japelj, J., Vergani, S. D., Salvaterra, R., et al. 2016, A&A, 590, A129
Jenkins, E. B. 2009, ApJ, 700, 1299
Kashino, D., Lilly, S. J., Renzini, A., et al. 2022, ApJ, 925, 82
Kashino, D., Renzini, A., Silverman, J. D., & Daddi, E. 2016, ApJ, 823, L24
Katz, H., Liu, S., Kimm, T., et al. 2022, PRISM: A Non-Equilibrium, Multiphase Interstellar Medium Model for Radiation Hydrodynamics Simulations of Galaxies
Katz, H., Saxena, A., Cameron, A. J., et al. 2023, MNRAS, 518, 592
Kennicutt, Robert C., J. & Evans, Neal J., I. 2012, ARA&A, 50, 531
Kewley, L. J. & Ellison, S. L. 2008, ApJ, 681, 1183
Kewley, L. J., Nicholls, D. C., & Sutherland, R. S. 2019, ARA&A, 57, 511
Khusanova, Y., Bethermin, M., Le Fèvre, O., et al. 2021, A&A, 649, A152
Kippenhahn, R., Weigert, A., & Weiss, A. 2012, Stellar Structure and Evolution, 2nd edn. (Springer)
Klencki, J. & Metzger, B. D. 2025, arXiv e-prints, arXiv:2510.09745
Klencki, J., Moe, M., Gladysz, W., et al. 2018, A&A, 619, A77
Knowles, A. T., Sansom, A. E., Vazdekis, A., & Allende Prieto, C. 2023, MNRAS, 523, 3450
Kobayashi, C., Leung, S.-C., & Nomoto, K. 2020, ApJ, 895, 138
Kobayashi, C. & Taylor, P. 2023, arXiv e-prints, arXiv:2302.07255
Konstantopoulou, C., De Cia, A., Krogager, J.-K., et al. 2024, A&A, 691, A129
Kotiwale, G., Matthee, J., Kashino, D., et al. 2026, A&A, 706, A165
Kovlakas, K., Zezas, A., Andrews, J. J., et al. 2020, MNRAS, 498, 4790
Krogager, J.-K., De Cia, A., Heintz, K. E., et al. 2024, MNRAS, 535, 561
Kroupa, P. 2001, MNRAS, 322, 231
Krtička, J. & Kubát, J. 2018, A&A, 612, A20
Kruijssen, J. M. D. 2025, arXiv e-prints, arXiv:2501.16438
Krumholz, M. R., McKee, C. F., & Bland-Hawthorn, J. 2019, ARA&A, 57, 227
Kudritzki, R. P. 2002, ApJ, 577, 389
Lagos, C. d. P., Theuns, T., Schaye, J., et al. 2016, MNRAS, 459, 2632
Langer, N. 2012, ARA&A, 50, 107
Langer, N. & Norman, C. A. 2006, ApJ, 638, L63
Langeroodi, D. & Hjorth, J. 2023, arXiv e-prints, arXiv:2307.06336
Lara-López, M. A., Cepa, J., Bongiovanni, A., et al. 2010, A&A, 521, L53
Laseter, I. H., Maseda, M. V., Bunker, A. J., et al. 2025, arXiv e-prints, arXiv:2510.15024
Laseter, I. H., Maseda, M. V., Curti, M., et al. 2024, A&A, 681, A70
Legnardi, M. V., Milone, A. P., Armillotta, L., et al. 2022, MNRAS, 513, 735
Legnardi, M. V., Milone, A. P., Cordoni, G., et al. 2024, A&A, 687, A160
Lehmer, B. D., Eufrasio, R. T., Basu-Zych, A., et al. 2021, ApJ, 907, 17
Leitherer, C., Schaerer, D., Goldader, J. D., et al. 1999, ApJS, 123, 3
Leja, J., van Dokkum, P. G., Franx, M., & Whitaker, K. E. 2015, ApJ, 798, 115
LIGO Scientific Collaboration, Virgo Collaboration, & KAGRA Collaboration. 2025, arXiv e-prints [arXiv:2508.18082]
Livio, M. & Mazzali, P. 2018, Phys. Rep., 736, 1
Lodders, K., Palme, H., & Gail, H. P. 2009, Landolt-Börnstein, 4B, 712
Loiacono, F., Decarli, R., Gruppioni, C., et al. 2021, A&A, 646, A76
Lunnan, R., Chornock, R., Berger, E., et al. 2014, ApJ, 787, 138
Madau, P. & Dickinson, M. 2014, ARA&A, 52, 415
Madau, P. & Fragos, T. 2017, ApJ, 840, 39
Maiolino, R. & Mannucci, F. 2019, A&A Rev., 27, 3
Maiolino, R., Nagao, T., Grazian, A., et al. 2008, A&A, 488, 463
Mandel, I. & de Mink, S. E. 2016, MNRAS, 458, 2634
Mannucci, F., Cresci, G., Maiolino, R., Marconi, A., & Gnerucci, A. 2010, MNRAS, 408, 2115
Mannucci, F., Salvaterra, R., & Campisi, M. A. 2011, MNRAS, 414, 1263
Maoz, D. & Mannucci, F. 2012, PASA, 29, 447
Maoz, D., Mannucci, F., & Nelemans, G. 2014, ARA&A, 52, 107
Marchant, P., Langer, N., Podsiadlowski, P., Tauris, T. M., & Moriya, T. J. 2016, A&A, 588, A50
Martins, F., Palacios, A., Schaerer, D., & Marques-Chaves, R. 2025, A&A, 698, A262
Martis, N., Withers, S., Felicioni, G., et al. 2025, arXiv e-prints, arXiv:2503.01579
Massari, D. 2025, RNAAS, 9, 64
Massari, D., Koppelman, H. H., & Helmi, A. 2019, A&A, 630, L4
Matteucci, F. 2021, A&A Rev., 29, 5
Matteucci, F. & Greggio, L. 1986, A&A, 154, 279
Matthee, J. & Schaye, J. 2018, MNRAS, 479, L34
McAlpine, S., Helly, J. C., Schaller, M., et al. 2016, Astronomy and Computing, 15, 72
McKenzie, M. & Bekki, K. 2021, MNRAS, 507, 834
Mérida, R. M., Pérez-González, P. G., Sánchez-Blázquez, P., et al. 2023, ApJ, 950, 125
Merritt, J., Stevenson, S., Sander, A., et al. 2025, arXiv e-prints, arXiv:2507.17052
Meynet, G., Chomienne, V., Ekström, S., et al. 2015, A&A, 575, A60
Monty, S., Belokurov, V., Sanders, J. L., et al. 2024, MNRAS, 533, 2420
Monty, S., Strom, A. L., Stanton, T. M., et al. 2025, MNRAS, 542, 1443
Monty, S., Yong, D., Marino, A. F., et al. 2023, MNRAS, 518, 965
Morishita, T., Stiavelli, M., Grillo, C., et al. 2024, ApJ, 971, 43
Muraveva, T., Giannetti, A., Clementini, G., Garofalo, A., & Monti, L. 2025, MNRAS, 536, 2749
Muzzin, A., Marchesini, D., Stefanon, M., et al. 2013, ApJ, 777, 18
Nakajima, K., Ouchi, M., Isobe, Y., et al. 2023, ApJS, 269, 33
Nakajima, K., Ouchi, M., Xu, Y., et al. 2022, ApJS, 262, 3
Narloch, W., Pietrzyński, G., Gieren, W., et al. 2021, A&A, 647, A135
Navarro-Carrera, R., Rinaldi, P., Caputi, K. I., et al. 2024, ApJ, 961, 207
Neijssel, C. J., Vigna-Gómez, A., Stevenson, S., et al. 2019, MNRAS, 490, 3740
Nelson, D., Springel, V., Pillepich, A., et al. 2019, Computational Astrophysics and Cosmology, 6, 2

Nissen, P. E. 2015, A&A, 579, A52
Nomoto, K. 1982, ApJ, 253, 798
Nomoto, K., Iwamoto, K., Nakasato, N., et al. 1997, Nucl. Phys. A, 621, 467
Park, M., Conroy, C., Johnson, B. D., et al. 2025, ApJ, 994, 165
Patel, S. G., Fumagalli, M., Franx, M., et al. 2013, ApJ, 778, 115
Pauldrach, A. W. A., Feldmeier, A., Puls, J., & Kudritzki, R. P. 1993, Space Sci. Rev., 66, 105
Perley, D. A., Tanvir, N. R., Hjorth, J., et al. 2016, ApJ, 817, 8
Pietrinferni, A., Cassisi, S., Salaris, M., Percival, S. B., & Ferguson, J. W. 2009, ApJ, 697, 275
Pietrinferni, A., Hidalgo, S., Cassisi, S., et al. 2021, ApJ, 908, 102
Pillepich, A., Springel, V., Nelson, D., et al. 2018, MNRAS, 473, 4077
Popesso, P., Concas, A., Cresci, G., et al. 2023, MNRAS, 519, 1526
Puls, J., Vink, J. S., & Najarro, F. 2008, A&A Rev., 16, 209
Reina-Campos, M., Keller, B. W., Kruijssen, J. M. D., et al. 2022, MNRAS, 517, 3144
Renaud, F. 2018, New A Rev., 81, 1
Revalski, M., Rafelski, M., Henry, A., et al. 2024, ApJ, 966, 228
Richings, A. J., Schaye, J., & Oppenheimer, B. D. 2014, MNRAS, 440, 3349–3369
Rinaldi, P., Caputi, K. I., van Mierlo, S. E., et al. 2022, ApJ, 930, 128
Rinaldi, P., Navarro-Carrera, R., Caputi, K. I., et al. 2025, ApJ, 981, 161
Rodighiero, G., Daddi, E., Baronchelli, I., et al. 2011, ApJ, 739, L40
Romagnolo, A., Gormaz-Matamala, A. C., & Belczynski, K. 2024, ApJ, 964, L23
Romaniello, M., Primas, F., Mottini, M., et al. 2008, A&A, 488, 731
Runco, J. N., Shapley, A. E., Sanders, R. L., et al. 2021, MNRAS, 502, 2600
Sabhahit, G. N., Vink, J. S., Sander, A. A. C., & Higgins, E. R. 2023, MNRAS, 524, 1529
Saccardi, A., Vergani, S. D., De Cia, A., et al. 2023, A&A, 671, A84
Saccardi, A., Vergani, S. D., Izzo, L., et al. 2025, arXiv e-prints, arXiv:2506.04340
Sánchez-Menguiano, L., Sánchez, S. F., Pérez, I., et al. 2017, A&A, 603, A113
Sánchez-Menguiano, L., Sánchez, S. F., Pérez, I., et al. 2016, A&A, 587, A70
Sanders, R. L., Shapley, A. E., Jones, T., et al. 2021, ApJ, 914, 19
Sanders, R. L., Shapley, A. E., Kriek, M., et al. 2018, ApJ, 858, 99
Sanders, R. L., Shapley, A. E., Topping, M. W., Reddy, N. A., & Brammer, G. B. 2024, ApJ, 962, 24
Sargent, M. T., Béthermin, M., Daddi, E., & Elbaz, D. 2012, ApJ, 747, L31
Schaerer, D., Fragos, T., & Izotov, Y. I. 2019, A&A, 622, L10
Schaye, J., Crain, R. A., Bower, R. G., et al. 2015, MNRAS, 446, 521
Schneider, F. R. N., Podsiadlowski, P., & Müller, B. 2021, A&A, 645, A5
Scholte, D., Saintonge, A., Moustakas, J., et al. 2024, MNRAS, 535, 2341
Schreiber, C., Pannella, M., Elbaz, D., et al. 2015, A&A, 575, A74
Schulze, S., Krühler, T., Leloudas, G., et al. 2018, MNRAS, 473, 1258
Senchyna, P., Stark, D. P., Vidal-García, A., et al. 2017, MNRAS, 472, 2608
Sesar, B., Banholzer, S. R., Cohen, J. G., et al. 2014, ApJ, 793, 135
Sharda, P., Amarsi, A. M., Grasha, K., et al. 2023, MNRAS, 518, 3985
Simmonds, C., Tacchella, S., McClymont, W., et al. 2025, arXiv e-prints, arXiv:2508.04410
Smith, L. J., Norris, R. P. F., & Crowther, P. A. 2002, MNRAS, 337, 1309
Smith, N. 2014, ARA&A, 52, 487
Speagle, J. S., Steinhardt, C. L., Capak, P. L., & Silverman, J. D. 2014, ApJS, 214, 15
Spina, L., Ting, Y. S., De Silva, G. M., et al. 2021, MNRAS, 503, 3279
Stanton, T. M., Cullen, F., McLure, R. J., et al. 2024, MNRAS, 532, 3102
Stanway, E. R. & Eldridge, J. J. 2018, MNRAS, 479, 75
Stanway, E. R., Eldridge, J. J., & Becker, G. D. 2016, MNRAS, 456, 485
Stefanon, M., Bouwens, R. J., Labbé, I., et al. 2021, ApJ, 922, 29
Steidel, C. C., Strom, A. L., Pettini, M., et al. 2016, ApJ, 826, 159
Stevenson, S., Sampson, M., Powell, J., et al. 2019, ApJ, 882, 121
Strom, A. L., Rudie, G. C., Steidel, C. C., & Trainor, R. F. 2022, ApJ, 925, 116
Strom, A. L., Steidel, C. C., Rudie, G. C., Trainor, R. F., & Pettini, M. 2018, ApJ, 868, 117
Strom, A. L., Steidel, C. C., Rudie, G. C., et al. 2017, ApJ, 836, 164
Szécsi, D., Langer, N., Yoon, S.-C., et al. 2015, A&A, 581, A15
Tanvir, N. R., Fox, D. B., Levan, A. J., et al. 2009, Nature, 461, 1254
Telford, O. G., Badenes, C., Eldridge, J. J., Stanway, E. R., et al. 2023, ApJ, 943, 65
Telford, O. G., Dalcanton, J. J., Skillman, E. D., & Conroy, C. 2016, ApJ, 827, 35
Thomas, D. & Maraston, C. 2003, A&A, 401, 429
Tinsley, B. M. 1979, ApJ, 229, 1046
Tomczak, A. R., Quadri, R. F., Tran, K.-V. H., et al. 2016, ApJ, 817, 118
Topping, M. W., Shapley, A. E., Reddy, N. A., et al. 2020, MNRAS, 495, 4430
Torrey, P., Vogelsberger, M., Hernquist, L., et al. 2018, MNRAS, 477, L16
Trager, S. C., Faber, S. M., Worthey, G., & González, J. J. 2000, AJ, 119, 1645
Trainor, R. F., Strom, A. L., Steidel, C. C., & Rudie, G. C. 2016, ApJ, 832, 171
Tremonti, C. A., Heckman, T. M., Kauffmann, G., et al. 2004, ApJ, 613, 898
VandenBerg, D. A., Bergbusch, P. A., Dotter, A., et al. 2012, ApJ, 755, 15
VandenBerg, D. A., Brogaard, K., Leaman, R., & Casagrande, L. 2013, ApJ, 775, 134
Vazdekis, A., Coelho, P., Cassisi, S., et al. 2015, MNRAS, 449, 1177
Vergani, S. D., Salvaterra, R., Japelj, J., et al. 2015, A&A, 581, A102
Vink, J. S. 2022, ARA&A, 60, 203
Vink, J. S. & de Koter, A. 2005, A&A, 442, 587
Vink, J. S., de Koter, A., & Lamers, H. J. G. L. M. 2001, A&A, 369, 574
Vink, J. S., Muijres, L. E., Anthonisse, B., et al. 2011, A&A, 531, A132
Vink, J. S., Sabhahit, G. N., Higgins, E. R., et al. 2024, A&A, 689, A24, see also arXiv:2407.07204
Vink, J. S. & Sander, A. A. C. 2021, MNRAS, 504, 2051
Virtanen, P., Gommers, R., Oliphant, T. E., et al. 2020, Nature Methods, 17, 261
Vreeswijk, P. M., Ellison, S. L., Ledoux, C., et al. 2004, A&A, 419, 927
Wallerstein, G. 1962, ApJS, 6, 407
Wang, B. & Han, Z. 2012, New A Rev., 56, 122
Webbink, R. F. 1984, ApJ, 277, 355
Weibel, A., Oesch, P. A., Barrufet, L., et al. 2024, MNRAS, 533, 1808
Weinberger, R., Springel, V., Hernquist, L., et al. 2017, MNRAS, 465, 3291
Wheeler, J. C., Sneden, C., & Truran, Jr., J. W. 1989, ARA&A, 27, 279
Whitler, L., Stark, D. P., Topping, M. W., et al. 2025, arXiv e-prints, arXiv:2501.00984
Woosley, S. E. & Heger, A. 2006, ApJ, 637, 914
Woosley, S. E., Heger, A., & Weaver, T. A. 2002, Rev. Mod. Phys., 74, 1015
Xin, C., Renzo, M., & Metzger, B. D. 2022, MNRAS, 516, 5816
Yates, R. M., Kauffmann, G., & Guo, Q. 2012, MNRAS, 422, 215
Yoon, S. C. & Langer, N. 2005, A&A, 443, 643
Yoon, S.-C., Langer, N., & Norman, C. 2006, A&A, 460, 199

Appendix A: Metallicity-dependent cosmic star formation history from galaxy scaling relations

We model all distributions as (log)normal

$$\mathcal{N}(x;\mu,\sigma) = \frac{1}{\sqrt{2\pi}\sigma}\exp\left[-\frac{(x-\mu)^2}{2\sigma^2}\right]. \tag{A.1}$$

where μ represents the mean and σ dispersion.
At fixed galaxy stellar mass M_* and redshift z, the SFR distribution is centred on the SFMR (Sect. A.2):

$$P(\log_{10}\mathrm{SFR}\,|\,M_*,z) = \mathcal{N}(\log_{10}\mathrm{SFR}_{\mathrm{SFMR}}(M_*,z),\sigma_{\mathrm{SFR}})\,. \tag{A.2}$$

with $\sigma_{\mathrm{SFR}} = 0.3$ dex. In presence of the SB sequence (Sect. A.6), it becomes bimodal:

$$\begin{aligned} P(\log_{10}\mathrm{SFR}\,|\,M_*,z) &= [1-f_{\mathrm{SB}}(M_*,z)] \\ &\times\mathcal{N}(\log_{10}\mathrm{SFR}_{\mathrm{SFMR}}(M_*,z),\sigma_{\mathrm{SFR}}) \\ &+f_{\mathrm{SB}}(M_*,z)\mathcal{N}(\log_{10}\mathrm{SFR}_{\mathrm{SB}}(M_*,z),\sigma_{\mathrm{SB}})\,, \end{aligned} \tag{A.3}$$

with σ_{SB}=0.2 dex and the relative SB and SFMR occupation governed by the SB fraction f_{SB}. Oxygen abundance distribution is centred on the value assigned using the FMR (Sect. A.4):

$$P(Z_{\mathrm{O/H}}|M_*,\mathrm{SFR},z) = \mathcal{N}(Z_{\mathrm{O/H;FMR}}(M_*,\mathrm{SFR},z),\sigma_{\mathrm{FMR}})\,, \tag{A.4}$$

with σ_{FMR}=0.05 dex. The oxygen-based metallicity-dependent cSFH can be written as

$$\begin{aligned} f_{\mathrm{SFR}}(Z_{\mathrm{O/H}},z) &= \int d\log_{10}M_*\,\frac{dn_{\mathrm{gal}}}{d\log_{10}M_*}(z) \\ &\int d\log_{10}\mathrm{SFR}\;P(\log_{10}\mathrm{SFR}\,|\,M_*,z)\;\mathrm{SFR} \\ &\times P_\nabla(Z_{\mathrm{O/H}}\,\big|\,Z_{\mathrm{O/H;FMR}}(M_*,\mathrm{SFR},z))\,, \end{aligned} \tag{A.5}$$

where $\frac{dn_{\mathrm{gal}}}{d\log_{10}M_*}$ follows from the GSMF (Sect. A.5) and

$$P_\nabla(Z_{\mathrm{O/H}}\,\big|\,Z_{\mathrm{O/H;FMR}}) = \mathcal{N}(Z_{\mathrm{O/H}},Z_{\mathrm{O/H;FMR}},\sigma_{\nabla\mathrm{O/H}}) \tag{A.6}$$

represents additional spread in star formation over metallicity inside galaxies, modelled as a normal distribution in $Z_{\mathrm{O/H}}$ centred on the FMR value.
Analogously, the iron-based cSFH can be written as

$$\begin{aligned} f_{\mathrm{SFR}}(Z_{\mathrm{Fe/H}},z) &= \int d\log_{10}M_*\,\frac{dn_{\mathrm{gal}}}{d\log_{10}M_*}(z) \\ &\int d\log_{10}\mathrm{SFR}\;P(\log_{10}\mathrm{SFR}\,|\,M_*,z)\;\mathrm{SFR} \\ &\times P_\nabla\left(Z_{\mathrm{Fe/H}}\,\big|\,Z_{\mathrm{Fe/H,avg}}\right), \end{aligned} \tag{A.7}$$

where

$$Z_{\mathrm{Fe/H,avg}} = Z_{\mathrm{O/H,FMR}} - [\mathrm{O/Fe}]_{\mathrm{avg}} - \log_{10}(\mathrm{O/Fe})_\odot, \tag{A.8}$$

and $[\mathrm{O/Fe}]_{\mathrm{avg}}$ follows from the [O/Fe]–sSFR relation, and

$$P_\nabla\left(Z_{\mathrm{Fe/H}}\,\big|\,Z_{\mathrm{Fe/H,avg}}\right) = \mathcal{N}\left(Z_{\mathrm{Fe/H}},Z_{\mathrm{Fe/H;avg}},\sigma_{\nabla\mathrm{Fe/H}}\right). \tag{A.9}$$

Similarly, one can compute the cSFH as a function of the oxygen over iron abundance ratio:

$$\begin{aligned} f_{\mathrm{SFR}}([\mathrm{O/Fe}],z) &= \int d\log_{10}M_*\,\frac{dn_{\mathrm{gal}}}{d\log_{10}M_*}(z) \\ &\int d\log_{10}\mathrm{SFR}\;P(\log_{10}\mathrm{SFR}\,|\,M_*,z)\;\mathrm{SFR} \\ &\times P\left([\mathrm{O/Fe}]\,\big|\,[\mathrm{O/Fe}]_{avg}\right), \end{aligned} \tag{A.10}$$

and we introduce additional scatter in [O/Fe] to account for possible inhomogeneities in local O and Fe enrichment within galaxies:

$$P\left([\mathrm{O/Fe}]\,\big|\,[\mathrm{O/Fe}]_{avg}\right) = \mathcal{N}\left([\mathrm{O/Fe}],[\mathrm{O/Fe}]_{\mathrm{avg}},\sigma_{\mathrm{O/Fe}}\right). \tag{A.11}$$

We assume $\sigma_{\nabla\mathrm{O/H}} = \sigma_{\nabla\mathrm{Fe/H}}$=0.14 dex and $\sigma_{\mathrm{O/Fe}} = 0.25\cdot\sigma_{\nabla\mathrm{O/H}}$ (see Sect. C).

The cosmic star formation rate density within a given metallicity interval $\Delta Z_X = Z_{X;\max} - Z_{X;\min}$ is then given by

$$\mathrm{SFRD}(\Delta Z_X,z) = \int_{Z_{X;\min}}^{Z_{X;\max}} f_{\mathrm{SFR}}(Z_X,z),dZ_X. \tag{A.12}$$

Here, Z_X denotes any of the metallicity tracers considered above (oxygen abundance, iron abundance, or [O/Fe]). The total cSFH is recovered by integrating over the full metallicity range. In our numerical framework, A.5, A.7 and A.10 integrals are discretised and evaluated over grids in mass, metallicity (200 equally spaced bins in $Z_{O/H}$ between 5.3 and 9.7, in [Fe/H] between -4.3 and 2.3, in [O/Fe] between -0.3 and 0.8) and cosmic time $t(z\leq 10)$ in 60 Myr intervals, where we sum contributions from galaxies with $\log_{10}M_*\in[6,12]$. Stellar mass density formed outside the metallicity grid is assigned to the nearest edge bin.

A.1. Galaxy scaling relations

Galaxy scaling relations (SFMR, MZR, and FMR) are described with a common functional form:

$$\log Y = \log Y_{\mathrm{asym}}(x) - B(x)\log_{10}\left[1+\left(\frac{M_*}{M_0(x)}\right)^{-a/B(x)}\right], \tag{A.13}$$

where a is the low-mass slope, M_0 is the turnover mass, $\log Y_{\mathrm{asym}}$ is the asymptotic high-mass value, B controls the width of the turnover and x denotes a potential secondary dependence on redshift/cosmic time or SFR.

A.2. Star formation–mass relation

The SFMR follows P23, Eq. (14)–(15):

$$\log_{10}\mathrm{SFR}_{\mathrm{SFMR}}(M_*,t) = a_0+a_1t_{Gyr}-\log_{10}\left[1+\left(\frac{M_*}{10^{a_2+a_3t_{Gyr}}}\right)^{-a_{SFR}}\right], \tag{A.14}$$

where t_{Gyr} is cosmic time in Gyr. The specific SFR of main sequence galaxies is then obtained as $\log_{10}\mathrm{sSFR}_{\mathrm{SFMR}}(M_*,t) = \log_{10}\mathrm{SFR}_{\mathrm{SFMR}}(M_*,t) - \log_{10}(\mathrm{M}_*)$. The SFMR parameters are

$$a_0 = 2.71,\quad a_1 = -0.186,\quad a_2 = 10.86,\quad a_3 = -0.0729, \tag{A.15}$$

and slope a_{SFR}=1 in P23. We consider an additional variation with a_{SFR}=0.8. We also consider a variation where coefficient that governs the dependence of the normalisation is set to a_1=-0.3 at $z\geqslant$1.8, leading to increased galaxy SFR at high z.

A.3. Mass–metallicity relation

The MZR,

$$Z_{\mathrm{O/H,MZR}} = Z_{\mathrm{O/H;MZR0}} - B_{\mathrm{MZR}}\log_{10}\left[1+\left(\frac{M_*}{M_{0;\mathrm{MZR0}}}\right)^{-a_{\mathrm{MZR}}/B_{\mathrm{MZR}}}\right],$$

(A.16)

is only evaluated at $z = 0$ with the parameters

$$a_{\rm MZR} = 0.28, \quad \log_{10} M_{0;\rm MZR0} = 10.02, \quad B_{\rm MZR} = 0.23, \quad (A.17)$$

as in Curti et al. (2020), and $Z_{\rm O/H;0}$=9 (shifted by +0.2 dex with respect to Curti et al. 2020).

A.4. Fundamental metallicity relation

The FMR follows phenomenological formulation from Ch21 (Eq. 1 - 6 therein, recalled below), and is parametrised as in Curti et al. (2020):

$$Z_{\rm O/H;FMR}({\rm SFR}, M_*) = Z_{\rm O/H;0} - \frac{\gamma_{FMR}}{\beta} \log_{10}\left[1 + \left(\frac{M_*}{M_{0;\rm SFR}}\right)^{-\beta}\right], \quad (A.18)$$

Ch21 defines the FMR parameters in terms of the $z = 0$ SFMR and MZR parameters and additional parameter $\nabla_{\rm FMR0}$, which characterises the strength of the SFR - $Z_{O/H}$ correlation in the low M_* regime as

$$\delta_{\rm MZR} = -\nabla_{\rm FMR0}\, \delta_{\rm SFMR}, \quad (A.19)$$

where

$$\delta_{\rm MZR} = Z_{\rm O/H,gal} - Z_{\rm O/H,MZR} \quad (A.20)$$

and

$$\delta_{\rm SFMR} = \log_{10}({\rm SFR_{gal}}) - \log_{10}({\rm SFR_{SFMR}}) \quad (A.21)$$

are the galaxy's offsets from the MZR and SFMR. The slope of the linear part of the FMR is defined as

$$\gamma_{\rm FMR} = a_{\rm MZR} + \nabla_{\rm FMR0}\, a_{\rm SFR}, \quad (A.22)$$

and the turnover mass depends on galaxy SFR

$$\log_{10} M_{0;\rm FMR}(\log_{10} {\rm SFR}) = \frac{\nabla_{\rm FMR0}}{\gamma_{\rm FMR}} \log_{10} {\rm SFR} - \frac{\nabla_{\rm FMR0}\, b_{\rm SFMR}}{\gamma_{\rm FMR}} + \frac{a_{\rm MZR}}{\gamma_{\rm FMR}} \log_{10} M_{0;\rm MZR0}, \quad (A.23)$$

where $b_{\rm SFR}$ is obtained from the linear low-mass part of the $z = 0$ SFMR,

$$\log_{10} {\rm SFR} = a_{\rm SFR} \log_{10} M_* + b_{\rm SFR}, \quad (A.24)$$

For the SFMR used in this study $b_{\rm SFR}$ follows from the P23 relation evaluated at t_0=$t_{Gyr}(z = 0)$

$$\log_{10} {\rm SFR} \simeq a_{SFR} \log_{10} M_* + [2.71 - 0.186\, t_0 - (10.86 - 0.0729\, t_0)]. \quad (A.25)$$

The FMR knee parameter $\beta(SFR)$ is evaluated numerically by enforcing that the FMR reproduces the $z = 0$ MZR for galaxies on the $z = 0$ SFMR. In the model variation with evolving FMR-normalisation we assume

$$Z_{\rm O/H;0}(z > 3) = -0.0357\,(z - 3) + Z_{\rm O/H;MZR0} \quad (A.26)$$

and use $Z_{\rm O/H;0} = Z_{\rm O/H;MZR0}$ otherwise.

Table A.1. Parameters from Eq. A.27, approximating the high-mass part of the GSMF.

z	$\log_{10}(\Phi_*/{\rm Mpc^{-3}dex^{-1}})$	$\log_{10}({\rm M_{GSMF}/M_\odot})$	$\alpha_{\rm high}$
0	-2.80	10.77	-1.32
1	-3.02	10.79	-1.34
2	-3.39	10.90	-1.37
3	-4.23	11.15	-1.66
4	-4.90	11.20	-1.95
5.5	-5.60	11.15	-2.25
7	-5.36	10.70	-2.1
8	-5.60	10.50	-1.98
9	-6.00	10.60	-1.98
10	-6.40	10.43	-1.99
11	-5.65	9.40	-2.01

A.5. Galaxy stellar mass function

The GSMF is obtained by averaging literature results grouped in several redshift bins, as detailed in ChN19. In addition to those listed in table 1 in ChN19, we include more recent works: Stefanon et al. (2021) (z=5.5-10.5), Hamadouche et al. (2024) (z=0.25-2.25), Navarro-Carrera et al. (2024) (z=3.5-8.5) and Weibel et al. (2024) (z=3.5-9.5). This more than doubles the number of GSMF estimates used at z>7.5, and leads to a more gradual evolution compared to ChN19, where the GSMF shows a sharp drop between z=7-8. At lower z the differences are minor. Following ChN19, we distinguish between the (Schechter-like) high-mass part of the GSMF and its power-law low-mass end. At $\log_{10}({\rm M_*}) \geqslant \log_{10}({\rm M_{lim}})$, the GSMF is described as

$$\Phi\,(M_*, z) = \ln(10)\,\Phi_* \left(\frac{M_*}{M_{\rm GSMF}}\right)^{\alpha_{\rm high}+1} \exp\left(-\frac{M_*}{M_{\rm GSMF}}\right), \quad (A.27)$$

where $\Phi\,(M_*, z) = \dfrac{dn_{\rm gal}}{d\log_{10} M_*}$.

Table A.1 summarises the parameters of a single Schechter function fits to the high-mass part of the GSMF used in this work. At $\log_{10}({\rm M_*}) < \log_{10}({\rm M_{lim}})$, the GSMF is described as a power-law with slope $\alpha_{\rm GSMF}$, i.e. $\Phi\,(M_*, z) \propto M_*^{\alpha_{GSMF}+1}$, and is normalised to ensure continuity with the high mass part. We assume $\log_{10}({\rm M_{lim}/M_\odot}) = 7.7 + 0.4z$ at z <4.5 and $\log_{10}({\rm M_{lim}/M_\odot})$=9.5 at z ≥4.5 and the slope $\alpha_{\rm GSMF}(z) = -1.4 - 0.08 \cdot z$, reaching $\alpha_{\rm GSMF}$=-2.2 at $z = 10$. Following ChN19, we contrast this with the variation in which the slope is fixed to $\alpha_{\rm GSMF} = \alpha_{\rm fix} = -1.45$, corresponding to the average literature value between z=0 and z=2. This serves to discuss the effect of low M_* extrapolation on our results. We extrapolate the GSMF down to $M_* = 10^6 M_\odot$, where it is essentially unconstrained, making it one of the main sources of uncertainty in $f_{\rm SFR}$(Z,z) at z ≳4 (ChN19; Ch21). The resulting GSMF is shown in the top panel of Fig. 1.

We do not extend our calculations beyond $z = 10.5$, except for extrapolating the cSFH trends shown in Fig. 7. For this purpose, we assume that at $z > 10.5$ the high-mass GSMF is fixed and we continue with the z-dependent low-mass end as described above. We warn that such extrapolation would lead to an increase in the SFRD at $z > 13$.

A.6. Starburst sequence

Following Ch21, in the negligible SB contribution variation we assume the SB sequence $\log_{10}{\rm SFR_{SB}}({\rm M_*, z}) = \log_{10}{\rm SFR_{SFMR}}({\rm M_*, z}) + \Delta_{\rm SB}$ with Δ_{SB}=0.59 dex, $\sigma_{\rm SB}$ = 0.2 dex

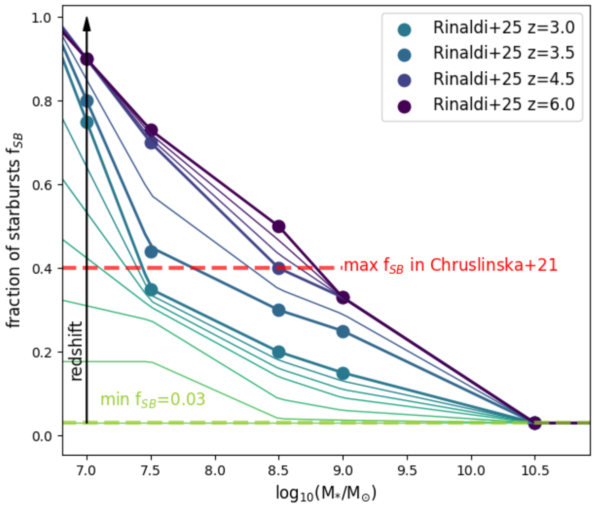

Fig. A.1. Fraction of starbursts as a function of galaxy stellar mass. The lines indicate redshifts between 0 and 6 in steps of 0.5. For $z < 3$ and $\log_{10}(M_*/M_\odot)>8$, the dependence is the same as in Ch21 but extended here to $z > 3$ and lower $\log_{10}(M_*)$ using the same approach. We adopt recent estimates from Rinaldi et al. (2025) (circles; see Fig. 5 therein).

and a fixed f_{SB}=0.03.
The high-SB scenario from Ch21 is based on the interpolation between the results from Bisigello et al. (2018) and Caputi et al. (2017) and fixed at $z > 4.4$ (exceeding z of their samples). The resulting f_{SB} increases to low M_* and high z up to f_{SB}=0.4, and the SB sequence is 1 dex above the SMFR. The work of Caputi et al. (2017) has recently been extended to $z \sim 6$ and low $M_* \lesssim 10^7 M_\odot$ by Rinaldi et al. (2022, 2025). They report further increase in f_{SB} with z and decreasing M_*, and the lack of a clear distinction between the SB and MS at low $\log_{10}(M_*/M_\odot)<7.5$. Rinaldi et al. (2025) suggest that the majority of the cosmic SFRD is produced by the SB galaxies. We modify the $f_{SB}(M_*, z)$ from Ch21 to include the results from Rinaldi et al. (2025) as shown in Fig. A.1 to comment on the impact of such a high SB contribution on our results. However, we assume the SB sequence is 1 dex above the SMFR. This is smaller than the offset between the peaks in the sSFR distribution of SB and MS galaxies in Rinaldi et al. (2025) (see Fig. 3 therein). Additionally, for variations with $a_{\rm SFR}<1$ (which is the case for Rinaldi et al. 2022, 2025), we require this offset to decrease linearly from 1 dex to 0 dex between $\log_{10}(M_*/M_\odot)=9$ and $\log_{10}(M_*/M_\odot)=6$. This is necessary to avoid drastically overestimating the cosmic SFRD($z > 2$) (right panel in Fig. 7, thick grey lines).
We note that in terms of the results presented in this paper, the high f_{SB} scenario described above would be indistinguishable from a scenario in which the SB sequence is absent and a_{SFR} is z-dependent (a_{SFR} ~0.9 at $z = 0$ and becomes $a_{SFR} \lesssim 0.8$ at $z > 2$).

Appendix B: Overview of model variations

Table B.1 summarises the variations of assumptions used to describe the statistical properties of the galaxies needed to derive $f_{\rm SFR}(Z_{O/H}, t)$ and $f_{\rm SFR}(Z_{Fe/H}, t)$ that were considered in this study.

Appendix C: Metallicity spread in galaxies

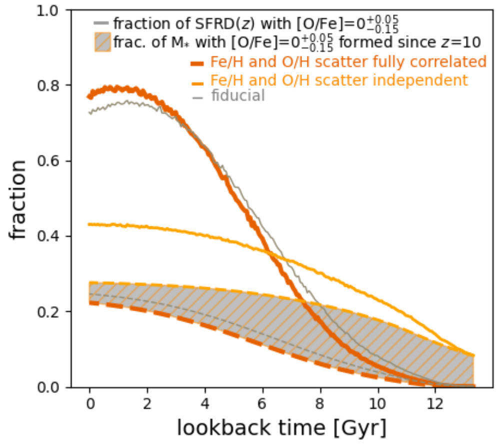

Fig. C.1. Effect of the assumed [O/Fe] scatter (relative to the fiducial case) on the estimated fraction of the SFRD forming with near-solar [O/Fe] (solid lines) and on the cumulative fraction of stellar mass formed with near-solar [O/Fe] since $z = 10$ (dashed lines and grey area). Larger scatter (the fully independent $Z_{\rm O/H}$ and $Z_{\rm Fe/H}$ case) increases these fractions, while smaller scatter (the fully correlated $Z_{\rm O/H}$ and $Z_{\rm Fe/H}$ case) decreases them.

The SFR within each 'galaxy' in our framework is distributed over a range of metallicities. As in ChN19, we model this as a normal distribution centred on the oxygen abundance $Z_{\rm O/H;FMR}$ assigned to a 'galaxy' based on the FMR (given SFR, M_*, and z), with dispersion $\sigma_{\nabla{\rm O/H}} = 0.14$ dex. This is a major simplification, but it does not significantly affect cosmic–volume–averaged results (e.g. metallicity–dependent cosmic SFH). ChN19 motivate this choice with the distribution of HII–region metallicities in $z \sim 0$ disk galaxies from CALIFA (Sánchez-Menguiano et al. 2016, 2017), which is roughly symmetric about the average value at the effective radius R_e; we take that average to represent the $Z_{\rm O/H}$ assigned via the scaling relations.
Here we further assume that $Z_{\rm Fe/H}$ within each 'galaxy' follows an analogous normal distribution with the same dispersion, $\sigma_{\nabla{\rm Fe/H}} = \sigma_{\nabla{\rm O/H}}$, centred on the value set by the [O/Fe]–sSFR relation and $Z_{\rm O/H;FMR}$ (Eq. A.8). This additional simplification is justified by the broadly comparable $Z_{\rm O/H}$ and $Z_{\rm Fe/H}$ gradients observed in galaxies (Hernandez et al. 2021).
One must still specify the spread in [O/Fe], $\sigma_{\rm O/Fe}$. If $Z_{\rm O/H}$ and $Z_{\rm Fe/H}$ with which the stars form inside a galaxy were fully correlated, then $\sigma_{\rm O/Fe} = 0$ and, at a given z, all of the SFR within a 'galaxy' would share a single [O/Fe]. If instead the two were uncorrelated (e.g. in a highly turbulent ISM mixing), then [O/Fe] would follow a normal distribution with $\sigma_{\rm O/Fe} = \sqrt{2} \times \sigma_{\nabla{\rm O/H}}$. Reality likely lies between these limits; for example, MW stars at fixed age, location, and [Fe/H] show a moderate spread in [O/H]. As our fiducial choice we adopt a weakly uncorrelated case, $\sigma_{\rm O/Fe} = \sigma_{\nabla{\rm O/H}}/4$. This choice is arbitrary, but it affects only $f_{\rm SFR}([{\rm O/Fe}], z)$ (see Eq. A.10) and results derived from it (Figs. 5, F.2, and F.3).
Figure C.1 illustrates the impact of $\sigma_{\rm O/Fe}$ on the fraction of the cosmic SFRD and the integrated stellar mass formed with near-solar [O/Fe] (as in the top panel of Fig. 5). The latter quantity is

Table B.1. Overview of the assumptions (model variations) considered in this study.

Variation	Notes
	[O/Fe] – sSFR relation (following Ch24; see Sect. 2.1)
'fast' Fe enrichment	$f_{Ia} \propto t^{-1}$, $\tau_{Ia;min}$=40 Myr, $m_{Fe}^{CCSN} = 0.03 M_\odot$
'mixed' Fe enrichment	f_{Ia} following Greggio (2010), $m_{Fe}^{CCSN} = 0.05 M_\odot$
'slow' Fe enrichment	$f_{Ia} \propto t^{-1}$, $\tau_{Ia;min}$=400 Myr, $m_{Fe}^{CCSN} = 0.1 M_\odot$
	SFMR/ galaxy main sequence
a_{SFR}=1	following Eq. 15 and table 2 in P23
a_{SFR}=0.8	P23 with shallower slope: parameter a4 in Table 2 in P23 set to 0.8
a_{SFR}=1 + evol.	P23 with faster evolution at $z > 1.8$: at $z \geqslant 1.8$ parameter a1 in Table 2 in P23 set to -0.3
	GSMF (following ChN19 with updates, see appendix A.5)
$\alpha_{GSMF}(z)$	low mass end slope steepening with z: $\alpha_{GSMF} = -1.4 - 0.08 \cdot z$
α_{GSMF} fixed	α_{GSMF}=-1.45
	MZR(z = 0) normalisation
$Z_{O/H;MZR0}$ = 9	fiducial value used here, following Curti et al. (2020) but shifted by +0.2 dex to match recombination line based estimates
$Z_{O/H;MZR0}$=8.8 - 9.1	range considered in Ch21, where relevant, we indicate how this would lead to a systematic shift in our results
	MZR(z=0)
-	Eq. 7 in Ch21 with a_{MZR}=0.28, β_{MZR}=0.23, $M_{0;MZR0}$ = 10.02 to match Curti et al. (2020), $Z_{O/H;MZR0}$ as above
	FMR($z > 3$)
fixed	redshift-invariant FMR modelled following Ch21
evol.	evolving normalisation at z >3, parameter $Z_{O/H;0}$ in Eq. 1 in Ch21 set to $Z_{O/H;0}(z > 3)$ = -0.0357 (z - 3) + $Z_{O/H;MZR0}$
	contribution of starbursts
negligible	following Ch21, fixed SB fraction f_{SB}=0.03, SB sequence 0.59 dex above the SFMR and scatter σ_{SB}=0.2 dex
high / high f_{SB}	see appendix A.6, based on Rinaldi et al. (2025) and considered only with a_{SFR}=1 SFMR variation

Notes. The combination of assumptions highlighted in bold corresponds to our example variation.

computed by evaluating Eq. C.1:

$$\frac{\int_{t(z=10)}^{t} \int_{-0.15+Z_{O/Fe\odot}}^{0.05+Z_{O/Fe\odot}} f_{SFR}(Z_{O/Fe}, t')\, dZ_{O/Fe}\, dt'}{\int_{t(z=10)}^{t} \int_{Z_{O/Fe;min}}^{Z_{O/Fe;max}} f_{SFR}(Z_{O/Fe}, t')\, dZ_{O/Fe}\, dt'} \tag{C.1}$$

where [O/Fe] = $Z_{O/Fe} - Z_{O/Fe,\odot}$. The integration limits in the numerator span oxygen-to-iron abundance ratios encompassing the range of solar values adopted in the literature, while the denominator covers the full range of galaxy $Z_{O/Fe}$ values. The cosmic time integral extends from the epoch corresponding to z = 10 (the maximum redshift considered in this work) to time t. The grey band in the top panel of Fig. 5 is obtained by evaluating Eq. C.1 across our model variations (Table B.1) assuming $\sigma_{O/Fe} = \sigma_{\nabla O/H}/4$ and it spans the full range of resulting values. In general, larger $\sigma_{O/Fe}$ broadens the distribution of [O/Fe] at a given epoch, increasing the fraction of stellar mass formed with near-solar [O/Fe] and leading to a weaker evolution of the instantaneous near-solar SFRD fraction over cosmic time. In Fig. C.1 we illustrate this effect for the model variation that maximises the near-solar [O/Fe] fraction (i.e. it sets the upper edge of the grey band in Fig. 5), obtaining a conservative upper bound of $\lesssim$ 30% on the fraction of stellar mass formed with near-solar [O/Fe] (dashed yellow line in Fig. C.1, obtained for $\sigma_{O/Fe} = \sqrt{2} \cdot \sigma_{\nabla O/H}$, corresponding to independent scatter in oxygen and iron). We therefore conclude that the specific treatment of scatter does not affect our main result that star formation with near-solar [O/Fe] is rare.

Appendix D: LGRB hosts: HI-weighted mean metallicity in redshift bins

Table D.1 summarises the HI column density-weighted mean metallicity in redshift bins for the sample of LGRB hosts discussed in Sect. 3.2.3.

Table D.1. N_{HI}-weighted mean metallicity from absorption-derived LGRB host properties.

selected subsample for which $[M/H]_{tot} \approx$ [Fe/H]				
z_{low}	z_{high}	number in bin	$\langle[Fe/H]\rangle_{HI}$	dispersion
1.7	2.1	6	-0.65	0.38
2.1	2.5	6	-1.01	0.46
2.5	2.95	5	-1.2	0.51
2.95	6.4	5	-1.69	0.23
all LGRBs				
z_{low}	z_{high}	number in bin	$\langle[M/H]\rangle_{HI}$	dispersion
1.7	2.2	9	-0.72	0.64
2.2	2.8	10	-1.01	0.47
2.8	3.8	9	-1.21	0.34
3.8	6.4	9	-1.18	0.68

Notes. See Sect. 3.2.3 and Fig. 9. The redshift bin edges (columns 1 and 2) were selected to ensure that each bin contains a similar number of LGRB hosts. Top rows: Subsample with dust corrections derived from Zn or accounting for α-enhancement for which $[M/H]_{tot}$ ≈[Fe/H]. Bottom rows: Also including objects with more approximate dust correction based on α-elements, in which case $[M/H]_{tot}$ may overestimate [Fe/H].

Appendix E: $Z_{O/H}$ and $Z_{Fe/H}$ metallicity distribution functions

In this section we compare the $f_{SFR}(Z_{Fe/H}, z)$ and $f_{SFR}(Z_{O/H}, z)$ integrated over z - i.e. the $Z_{Fe/H}$- and $Z_{O/H}$-MDFs. Figure E.1 shows the MDFs of stars formed between z = 0 and increasing z_x: the leftmost curves correspond to stars formed in the last ~1 Gyr, while the rightmost curves encompass the full ≈13.3 Gyr of cosmic history. For comparison, Fig. E.2 presents the complementary case, showing MDFs of stars formed between z = 10 and decreasing z_x, i.e. focusing on the early Universe. Together, these figures illustrate the buildup of the cosmic MDF, with the peak established at $z \lesssim 3$, where most of the cosmic stellar mass forms, and the low-metallicity tail developed at $z \gtrsim 2$ (cf. Fig. E.2). The brown/black ranges in Fig. E.1 span between the model variations and broaden with increasing z_x,

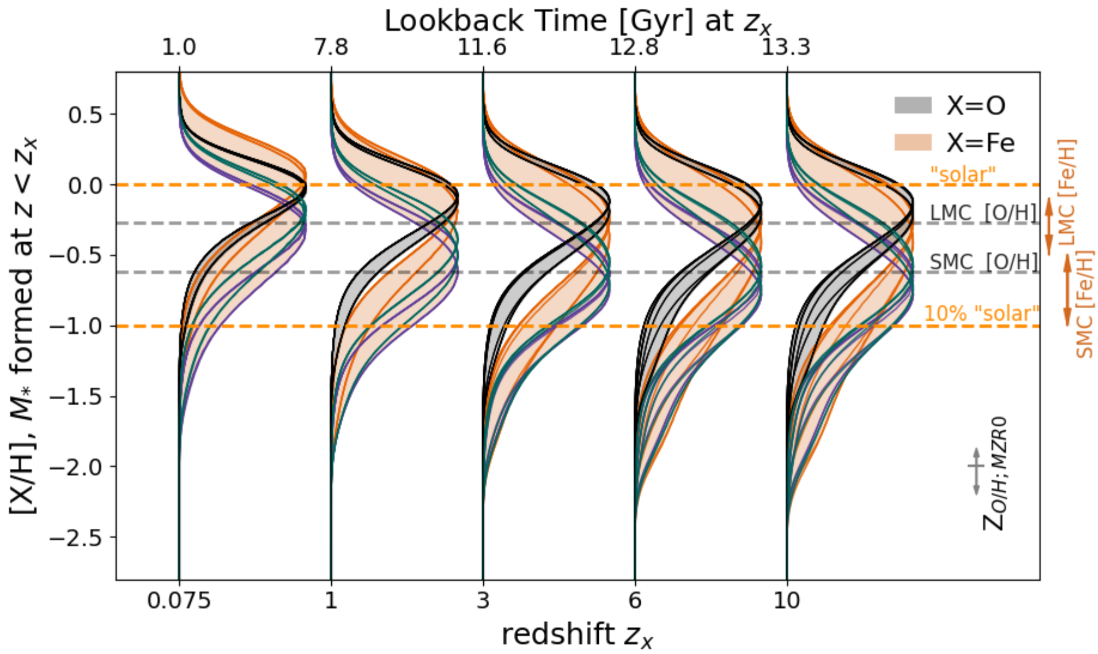

Fig. E.1. MDF of the stellar mass formed between $z = 0$ and z_x (as indicated on the horizontal axis), for [O/H] (grey bands, black curves) and [Fe/H] (brown bands, coloured curves). The colours distinguish the [O/Fe]–sSFR relation as in Fig. 2. the bands show the range for the individual model variations, which are shown as lines. the horizontal dashed lines mark solar, 0.1 solar, LMC and SMC [O/H] (Grevesse & Sauval 1998 reference scale). LMC and SMC [Fe/H] are marked as arrows. The grey arrows indicate the systematic uncertainty (unaccounted for in the plotted ranges) from the $Z_{O/H}$ calibration, which shifts all curves by a constant factor. All MDFs are normalised to unity to compare the shapes.

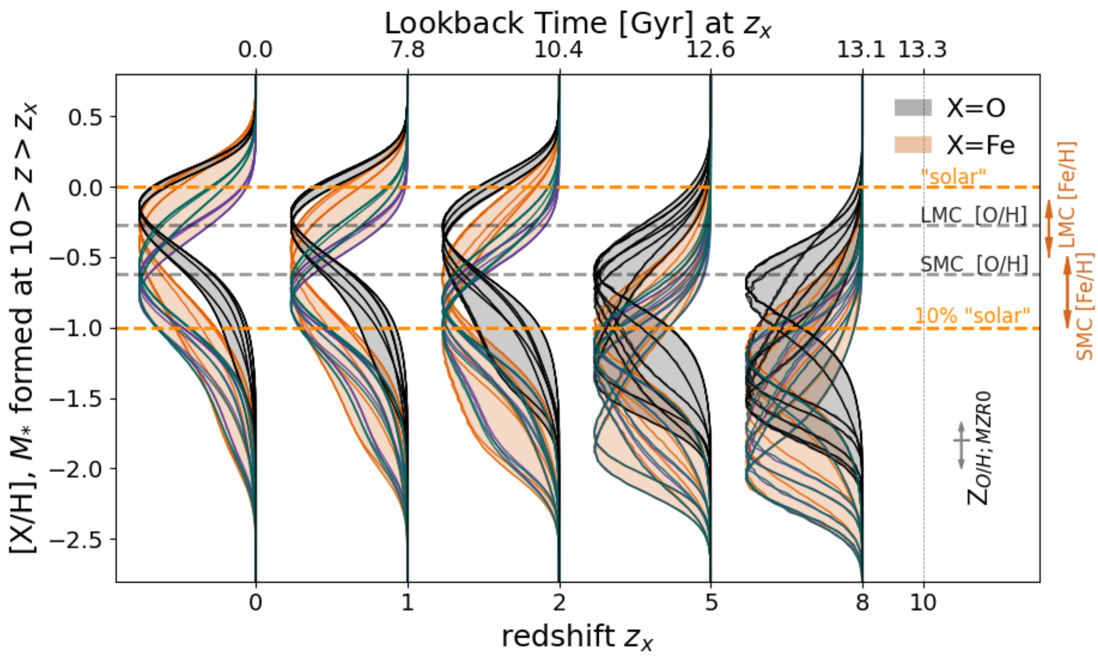

Fig. E.2. MDF of stellar mass formed between z_x (as indicated on the horizontal axis) and $z = 10$, for [O/H] (grey bands, black curves) and [Fe/H] (brown bands, coloured curves. The colours distinguish the [O/Fe]–sSFR relation as in Fig. 2. The bands show the range for the individual model variations, which are shown as lines. the horizontal dashed lines mark solar, 0.1 solar, and LMC/SMC [O/H] (reference scale (Grevesse & Sauval 1998)); LMC/SMC [Fe/H] are marked as arrows. The grey arrows indicate the systematic shifts from the $Z_{O/H}$ calibration.

reflecting the fact that our estimates are more uncertain at high z. As before, different assumptions about the [O/Fe]–sSFR relation (which affect only the $Z_{Fe/H}$-MDFs) are distinguished by colour. For stars formed in the last ∼1 Gyr, this assumption shifts the peak of the $Z_{Fe/H}$-MDF to higher (orange lines, 'fast' Fe enrichment) or lower (green/purple lines, 'mixed'/'slow' Fe enrichment) metallicities relative to solar and to the $Z_{O/H}$-MDF peak. The offset between the peaks reaches up to ∼0.3 dex for MDFs integrated over the past 1 Gyr and up to ≳0.5 dex when integrating over the full z range spanned by our models (with 'slow' Fe enrichment maximising the difference). For any fixed variation, the $Z_{Fe/H}$-MDF is broader than the corresponding $Z_{O/H}$-MDF.

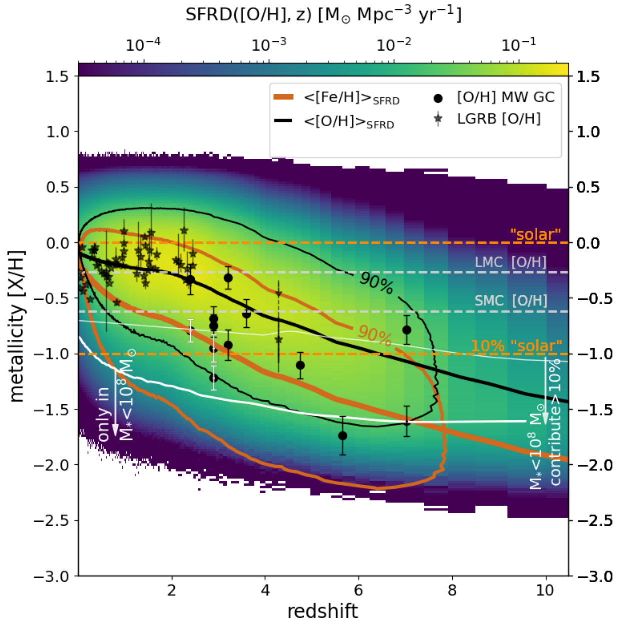

Fig. F.1. Distribution of the cosmic SFRD at different [O/H] and z (colour scale), shown for our example variation. The black and brown lines indicate the SFRD-weighted average [O/H] and [Fe/H] at each z, respectively. The solid white lines represent [O/H] below which $M_* < 10^8 M_\odot$ galaxies contribute at least 10% of the SFRD (thin line) and below which the contribution of $M_* > 10^8 M_\odot$ galaxies is negligible (thick line). The stars represent the [O/H] values for the individual LGRB hosts (Graham et al. 2023). The dots represent the [O/H] values for MW GCs. The [O/H] values for the LMC and SMC on our solar scale are indicated for reference.

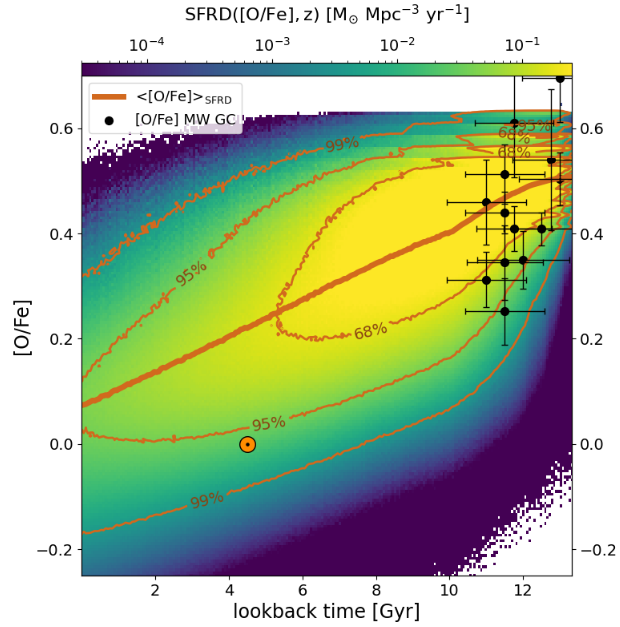

Fig. F.2. Distribution of the cosmic SFRD at different [O/Fe] and lookback times (colour scale), shown for our example variation, in particular, assuming the [O/Fe]–sSFR relation corresponding to our 'mixed Fe enrichment' case. The brown line represents the SFRD-weighted average [O/Fe] at each z. The contours enclose 68%, 95%, and 99% of the SFRD. The black dots represent the [O/Fe] values for the MW GCs. The orange dot marks the Sun's formation epoch at [O/Fe]=0 assuming the solar scale from Grevesse & Sauval (1998).

Aside from the impact of the [O/Fe]–sSFR relation (i.e. comparing curves of the same colour), differences appear mainly in the low-metallicity tails. This regime is dominated by contributions from low-M_* galaxies, where the associated uncertainties (parametrised by $a_{\rm SFR}$ and $\alpha_{\rm GSMF}$) accumulate in our model. We caution that all MDFs in Figs. E.2 and E.1 are normalised to unity to facilitate comparison of their shapes, but the total stellar mass formed differs across models (see Sect. 5.2). In particular, variations producing more extended low-metallicity tails generally also yield higher SFRDs (by a factor of ~2–3 at $z < 2$, and increasing to higher z), due to the larger contribution of low-M_* galaxies.

Appendix F: Additional figures

Figures F.1 and F.2 show the $f_{\rm SFR}([O/H], z)$ and $f_{\rm SFR}([O/Fe], t)$ distributions for our example variation, respectively. Figure F.3 shows the $f_{\rm SFR}([O/Fe], t)$ for the same variation but assuming a [O/Fe]-sSFR relation corresponding to our 'fast Fe enrichment' case. Figure E.2 shows the MDF of stellar mass formed between decreasing z thresholds and $z = 10$, i.e. complementary to Fig. E.1.

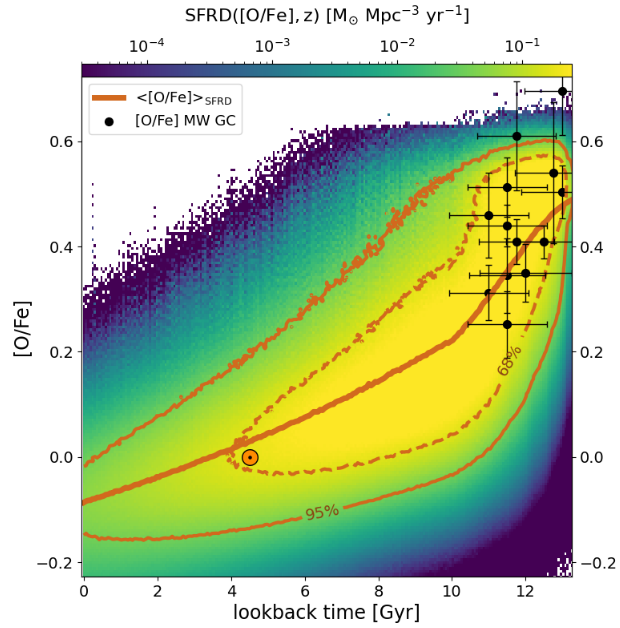

Fig. F.3. Same as Fig. F.2 but assuming the [O/Fe]–sSFR relation corresponding to our 'fast Fe enrichment' case.